

# PRISMS. UNCOVER-26185, a metal-poor SFG at $z=10.05$ with no evidence for a X-ray-luminous AGN

J. Álvarez-Márquez<sup>1\*</sup>, L. Colina<sup>1</sup>, A. Crespo-Gómez<sup>2</sup>, S. Kendrew<sup>3</sup>, J. Zavala<sup>4</sup>, R. Marques-Chaves<sup>5</sup>, C. Prieto-Jiménez<sup>1</sup>, Abdurro'uf<sup>6</sup>, C. Blanco-Prieto<sup>1</sup>, L. A. Boogaard<sup>7</sup>, M. Castellano<sup>8</sup>, A. Fontana<sup>8</sup>, Y. Fudamoto<sup>9</sup>, S. Fujimoto<sup>10,11</sup>, M. García-Marín<sup>3</sup>, Y. Harikane<sup>12</sup>, S. Harish<sup>2</sup>, T. Hashimoto<sup>13,14</sup>, T. Hsiao<sup>15</sup>, E. Iani<sup>16</sup>, A. K. Inoue<sup>17,18</sup>, D. Langeroodi<sup>19</sup>, R. Lin<sup>4</sup>, J. Melinder<sup>20</sup>, L. Napolitano<sup>8</sup>, G. Östlin<sup>20</sup>, P. G. Pérez-González<sup>1</sup>, P. Rinaldi<sup>21</sup>, B. Rodríguez Del Pino<sup>1</sup>, P. Santini<sup>8</sup>, Y. Sugahara<sup>17,18</sup>, T. Treu<sup>22</sup>, A. Varo-O'ferrall<sup>1</sup>, and G. Wright<sup>23</sup>

(Affiliations can be found after the references)

Received ; accepted

## ABSTRACT

This work presents the first results of the PRImordial galaxy Survey with MIRI Spectroscopy (PRISMS), a JWST cycle 4 program (PID 8051) aimed at the characterization of a relatively large sample of ten primordial galaxies about 500 Myr after the Big Bang. Here, we present deep (13.9 hours) spectroscopy with the MIRI Low-Resolution Spectrograph (LRS) of the lensed galaxy UNCOVER-26185 at a redshift of  $z=10.054\pm0.011$ . It is a faint UV galaxy ( $M_{\text{UV}}=-18.83\pm0.07$  mag) previously identified as a X-ray luminous active galactic nuclei. MIRI LRS detects the  $\text{H}\beta+[\text{OIII}]\lambda\lambda4960,5008\text{\AA}$  complex and  $\text{H}\alpha$  emission line with a significance of  $10\sigma$  and  $8\sigma$ , respectively, as well as the optical continuum emission at rest-frame  $0.45\text{\mu m}$  and  $0.57\text{\mu m}$  with a signal-to-noise ratio of 6–7. The UV-to-optical spectral energy distribution, combining continuum and emission lines, is compatible with: (i) a low stellar ( $A_V=0.2\pm0.09$ ) and nebular ( $A_V=0^{+0.4}_{-0.0}$ ) extinction, (ii) a star-formation history composed by a young ( $7\pm3$  Myr) starburst and an intermediate-age ( $65\pm20$  Myr) stellar population, and (iii) a total stellar mass of  $(1.7\pm0.3)\times10^8 M_{\odot}$ . The  $\text{H}\alpha$ -derived star-formation rate is  $\text{SFR}=1.3\pm0.3 M_{\odot}\text{ yr}^{-1}$  yielding a specific star formation rate of  $7.6\pm1.2\text{ Gyr}^{-1}$ . The low optical emission line ratios (e.g.,  $\log(\text{R23})=0.59\pm0.10$  and  $\log(\text{O32})=0.65\pm0.10$ ) locate UNCOVER-26185 as the most metal-poor galaxy ( $Z=0.04\pm0.01 Z_{\odot}$ ), and as outlier with the lowest ionization ( $\log U=-2.5$ ) identified so far at redshifts above 9. The measured low internal extinction, low ionization, and high  $\text{H}\alpha$  equivalent width ( $1399\pm271\text{\AA}$ ) do not support an scenario where the AGN is obscured by dust (host and torus) or by the BLR gas clouds, and alternative scenarios have to be considered. With no evidence of an active galactic nuclei in the rest-frame UV-to-optical spectrum, UNCOVER-26185 has the properties of a low-mass, metal-poor, main-sequence star-forming galaxy at redshift 10, with interstellar medium and ionization properties very different than those of the already studied UV-bright ( $M_{\text{UV}}<-20$  mag) galaxies at redshifts beyond 10 (e.g., GNz11, GHZ2, or JADES-GS-z14-0). PRISMS is starting to explore the population of intermediate-UV luminosity galaxies at  $z\sim10$ , covering UV absolute magnitudes in the range of  $-17.9\leq M_{\text{UV}}[\text{mag}]\leq-20.5$ , fainter than those of UV-bright galaxies studied so far.

**Key words.** Galaxies: high-redshift – Galaxies: starburst – Galaxies: ISM – Galaxies: individual: UNCOVER-26185

## 1. Introduction

JWST is revolutionizing our understanding of galaxy formation in the Epoch of Reionization (EoR) and beyond, pushing the spectroscopic detection frontier to redshifts slightly above 14, with galaxies such as JADES-GS-z14-0 (Carniani et al. 2024b; Schouws et al. 2025; Helton et al. 2025) and MoM-z14 (Naidu et al. 2025). NIRCam has identified several hundred photometric candidates at  $z\gtrsim10$  (Finkelstein et al. 2023; Pérez-González et al. 2023; Robertson et al. 2023), with tentative ones extending to  $z\sim17$  and even  $z\sim25$ –30 (e.g., Pérez-González et al. 2025; Castellano et al. 2025a), awaiting spectroscopic confirmation. To date, roughly fifty galaxies have been spectroscopically confirmed with NIRSpec in the first 500 Myr of the Universe (e.g., Curtis-Lake et al. 2023; Harikane et al. 2023; Arrabal Haro et al. 2023; Bunker et al. 2023; Roberts-Borsani et al. 2023; Hsiao et al. 2024a; Fujimoto et al. 2024; Castellano et al. 2024; Carniani et al. 2024b; Witstok et al. 2025; Napolitano et al. 2025a; Tang et al. 2025; Roberts-Borsani et al. 2025).

Some of these galaxies show signatures consistent with active black holes (BH, e.g., Kovács et al. 2024; Bogdán et al. 2024; Maiolino et al. 2024; Napolitano et al. 2025b), while

others resemble extreme, young, compact, low-metallicity starbursts (e.g., Hsiao et al. 2024b; Zavala et al. 2024; Álvarez-Márquez et al. 2025; Helton et al. 2025). The physical nature of these primordial galaxies, and the mechanisms driving their rapid stellar build-up and BH growth, remain the subject of intense debate. Proposed explanations span a wide range of scenarios, ranging from high star-formation efficiency in dense, metal-poor, feedback-free environments (Dekel et al. 2023), to the co-evolution of active galaxy nuclei (AGN) and star-formation (Ji et al. 2025). Others include dust-free conditions from strong radiation-driven outflows (Ferrara et al. 2023), top-heavy initial mass functions (Hutter et al. 2025), and stochastic star-forming histories (SFHs; Ciesla et al. 2024).

The limited spectral coverage of NIRCam and NIRSpec ( $<0.4\text{\mu m}$ ) at  $z\geq9.7$  biases our ability to reveal the nature of these galaxies. At such redshifts, key optical features— $\text{H}\alpha$  &  $[\text{OIII}]\lambda5008\text{\AA}$ , and their underlying continua—are redshifted into the Mid-Infrared Instrument (MIRI; Rieke et al. 2015; Wright et al. 2015, 2023) spectral range. To date, only four galaxies have reported detections of these lines—MACS0647-JD ( $z=10.2$ ; Hsiao et al. 2024b), GNz11 ( $z=10.6$ ; Álvarez-Márquez et al. 2025), GHZ2 ( $z=12.3$ ; Zavala et al. 2025), and JADES-GS-z14-0 ( $z=14.2$ ; Helton et al. 2025)—revealing: (i) the first direct- $T_{\text{e}}$

\* jalvarez@cab.inta-csic.es

metallicity ( $Z$ ) measurements at  $z > 10$ , showing relatively high metallicities of 10–20%  $Z_{\odot}$ , (ii) the lack of significant dust attenuation based on their Balmer decrements, (iii) elevated electron densities ( $n_e > 250 \text{ cm}^{-3}$ ) and temperatures ( $T_e \sim 1.5 \times 10^4 \text{ K}$ ), (iv) high photon production efficiencies ( $\log(\xi_{\text{ion}} [\text{Hz erg}^{-1}]) \geq 25.2$ ), and (v) the dominant starburst nature with high specific star formation (sSFR). These findings highlight the MIRI's pivotal role in constraining the nature and physical properties of these primordial galaxies. However, these studies have been limited so far to ultraviolet (UV) bright galaxies ( $M_{\text{UV}} < -21$ ).

A more comprehensive study into the nature and physical properties of these sources requires to enlarge the sample of  $z \sim 10$  galaxies with MIRI spectroscopy covering a wider range in  $M_{\text{UV}}$  to investigate their properties as a function of UV luminosity. The PRImordial galaxy Survey with MIRI Spectroscopy (PRISMS) program (PID 8051, PIs: J. Álvarez-Márquez and L. Colina) has selected a sample of ten spectroscopically confirmed galaxies ranging redshifts of  $9.7 < z < 10.4$  and UV absolute magnitudes of  $-17.9 \leq M_{\text{UV}} [\text{mag}] \leq -20.5$ , including lensed galaxies and AGN candidates.

The galaxy UNCOVER-26185 or UHz1 (hereafter U26185) is a member of the PRISMS galaxy sample that was first identified using deep NIRCam imaging as a high-redshift candidate galaxy with a photo- $z$  of 10.32 (Castellano et al. 2023b). NIRSpec spectroscopy follow-ups confirmed its high redshift at  $10.073 \pm 0.002$  based on the detection of several UV and optical emission lines (Goulding et al. 2023; Fujimoto et al. 2024). U26185 was detected as a strong X-ray source with the *Chandra* X-ray Observatory (Goulding et al. 2023; Bogdán et al. 2024). The lack of evidence of AGN features in the rest-frame UV has been interpreted as a heavily obscured luminous AGN hosting a  $10^7 - 10^8 M_{\odot}$  supermassive BH (SMBH) accreting at the Eddington rate. If confirmed, U26185 would represent one of the earliest SMBH detected so far, when the Universe was just about 500 Myr old favoring formation scenarios based on heavy seeds.

This paper presents the first results of the PRISMS project, where we analyze new MIRI spectroscopy, detecting the optical emission lines and underline continua, together with existing ancillary JWST and ALMA data for U26185. The paper is organized as follows. Section 2 introduces the MIRI observations and calibrations, together with the ancillary data. Section 3 presents the analysis of the MIRI observations, where fluxes of the emission lines and continuum are derived, together with the overall UV to far-infrared (FIR) spectral energy distribution (SED) fitting analysis. Section 4 shows the calculation of all physical properties, such as dust attenuation, SFH, ionizing photon production efficiency, ionization and emission line ratios, and metallicity. Section 5 discusses the nature of the ionized source. Section 6 concludes and summarizes the main results and discussions of the paper. Throughout this paper, we assume a Chabrier initial mass function (IMF, Chabrier 2003), vacuum emission line wavelengths, and a flat  $\Lambda$ CDM cosmology with  $\Omega_m = 0.310$ , and  $H_0 = 67.7 \text{ km s}^{-1} \text{ Mpc}^{-1}$  (Planck Collaboration et al. 2020).

## 2. Data and calibrations

### 2.1. MIRI LRS observations and calibrations

U26185 was observed with the Low Resolution Spectrograph (LRS, Kendrew et al. 2015) of MIRI on 19th and 20th of November of 2025 as part of the cycle 4 JWST program ID 8051 (PIs: J. Álvarez-Márquez & L. Colina). The MIRI LRS spectral coverage ranges from  $4.85 \mu\text{m}$  to  $14 \mu\text{m}$ , and uses a slit with a size of  $0.51 \times 4.7 \text{ arcsec}^2$ . It covers the optical rest-frame spectrum

of U26185, including bright optical emission lines, such as  $\text{H}\beta$ ,  $[\text{O III}]\lambda\lambda 4960, 5008 \text{ \AA}$ , and  $\text{H}\alpha$ , and their underlined continuum.

The MIRI LRS total on-source integration time corresponds to 49917 seconds (13.9 hours), distributed in 12 dither positions. Each dither uses 149 groups and 10 integrations in FASTR1 readout mode. We implement a non-standard four-point dither pattern. We combine a two-column mosaic and a two-point dither pattern. This strategy locates the target in four equidistant positions along the LRS slit instead of only two offered by the standard two-point dither pattern, and it is repeated 3 times to get the total number of dithers. This strategy allows a better mitigation of bad/hot pixels and pixels affected by cosmic rays, as well as an improvement on the background subtraction. A GAIA DR3 star is used to perform an offset target acquisition (TA) and locate our target in the center of the slit. The complementary verification LRS image confirms that the TA strategy works within subpixel uncertainties.

The LRS observations are processed with version 1.20.2 of the JWST calibration pipeline and context 1464 of the Calibration Reference Data System. We follow the standard MIRI LRS pipeline procedure (Bushouse et al. 2025), with additional customized steps to improve the quality of the final LRS calibrated products. We run the first and second stage of the pipeline following the default configuration, except for the jump step where we activate the `find_showers` keyword to search and correct the cosmic ray showers events. Before stage 3 and in the fully calibrated detector images, we implement four customized steps:

- Wavelength masking. We mask the calibrated detector image by assigning NaN values to pixels corresponding to wavelengths lower than  $4.85 \mu\text{m}$  and greater than  $8 \mu\text{m}$ , where no relevant spectral information is expected for this source.
- Master background correction. We generate a master background by performing a sigma-clipped median of all the calibrated detector masked images, independently of the pointing. That master background is individually subtracted from each of the detector images. The decision to subtract the background at the end of the second stage by the median of all the pointings is driven by the fact that the main source is not detected in individual exposures, and the noise is dominated by background and detector effects. Therefore, this pixel-by-pixel background subtraction would correct any optical or detector level residuals as well as any features and noise injected by the reference files (e.g. photometry and flat-field correction). A similar methodology has been already implemented in the calibration of deep MRS observations (e.g. Álvarez-Márquez et al. 2023, 2024).
- Residual background subtraction. Over the long exposure time (13.9 hours) of the LRS observation, the total background emission is seen to drift, causing changes in the background level between exposures. Also, scattering from the dispersed background in the MIRI Imager field causes spatial gradients in the slit region. The master background correction takes care of the mean background emission, but background residuals in the order of 1% compared to the total background are found between different observations. That residuals are in the range of the integrated fluxes of the  $\text{H}\beta + [\text{O III}]\lambda\lambda 4960, 5008 \text{ \AA}$  complex (hereafter  $\text{H}\beta + [\text{O III}]$ ) and  $\text{H}\alpha$  emission line, and a factor of about 10 higher than the continuum emission, being extremely important to correct it. Then, we perform a second order correction row by row (i.e., wavelength by wavelength), where we model the residual background emission in the spatial direction of the slit. We take each of the row of the detector image and:
- (i)

perform sigma clipping over the full row to remove outliers and pixels where the source emission is larger than  $3\sigma$ , (ii) smooth the flux values of the row (spatial direction of the slit) with a Gaussian filter, (iii) fit the smoothed row with a polynomial function, and (iv) subtract the derived polynomial function to the original row fluxes.

- Sigma clipping. We perform a sigma clipping over the masked and background subtracted calibrated image to remove any residual from bright cosmic rays, cosmic ray showers, and detector artifact. We have carefully checked that this step does not remove any flux from our target. In the case of U26185, the emission of the source is not detected over  $3\sigma$  in individual pointings.

Finally, we run the stage 3 of the pipeline to generate the combined 2D detector image and the 1D extracted spectrum (see left panels of Figure 1). The 1D extracted spectrum is calculated in an aperture with a diameter of 0.44 arcsec (dashed lines in left-upper panel of Figure 1). We implement aperture correction following the reference file in the JWST pipeline (e.g. `jwst_miri_apcorr_0017.fits`) and assuming a point-like source. Additionally, we extract two 1D background spectra from the full exposure time coverage of the 2D detector image to estimate the noise level (see orange dashed line in left-bottom panel of Figure 1).

## 2.2. Ancillary observations and absolute cross-instrument flux calibration

NIRCam imaging and NIRSpec spectroscopy data are publicly available in the UNCOVER project<sup>1</sup>. The NIRSpec R100 calibrated observations are obtained from the UNCOVER data release 4 (DR4; [Bezanson et al. 2024](#)). We use the NIRSpec 1D calibrated spectrum and emission lines fluxes derived by [Price et al. \(2025\)](#)<sup>2</sup>, together with the redshift ( $z = 10.061^{+0.011}_{-0.013}$ ). The NIRCam photometry, combining the medium and wide band filters, is obtained from the SUPER catalog of the UNCOVER DR3 ([Suess et al. 2024](#)). We also use the updated gravitational magnification from the UNCOVER DR4 ( $\mu = 4.07^{+0.03}_{-0.11}$ ; [Furtak et al. 2023](#); [Weaver et al. 2024](#); [Suess et al. 2024](#); [Price et al. 2025](#)). Finally, we include in the analysis the ALMA [OIII]88 $\mu$ m line and 90 $\mu$ m continuum emissions from [Algera et al. \(2025\)](#).

To correct unknown uncertainties in the calculation of the absolute slit path-losses of NIRSpec and MIRI spectra, we normalize both spectra to the NIRCam photometry. We first normalized NIRSpec to NIRCam photometry. We use the broad and medium band fluxes presented in Table 1 from the UNCOVER DR3 SUPER catalog, and generate synthetic NIRSpec photometry by integrating through the same filter transmission functions. We match both multi-band photometries, and derive a normalization factor of  $0.75 \pm 0.09$  for the NIRSpec spectra. NIRSpec emission lines fluxes from [Price et al. \(2025\)](#) are also normalized by the same factor, and presented in Table 1. MIRI LRS spectrum is normalized to the normalized NIRSpec spectrum as NIRCam or MIRI photometry is not available in the MIRI spectral range.

<sup>1</sup> UNCOVER webpage: <https://jwst-uncover.github.io/>

<sup>2</sup> UNCOVER DR4 and DJA V4 NIRSpec spectra are compatible, and the emission lines fluxes agree within  $1\sigma$ . DJA v4 include an extension of the wavelength up to 5.5  $\mu$ m, which covers the H $\beta$  emission line. The  $3\sigma$  upper-limit of the H $\beta$  flux is  $< 66 \times 10^{-20}$  erg s $^{-1}$  cm $^{-2}$ . We decide not to include that upper-limit in this work as the extension to longer wavelengths uses an extrapolated calibration. However, the value obtained is compatible with the H $\beta$ <sub>Case B</sub> used as fiducial in this work (see Sections 3.1 and 4.1).

**Table 1.** Magnified, scaled fluxes of all detected lines and continuum

MIRI LRS line fluxes [10 $^{-20}$ erg s $^{-1}$ cm $^{-2}$ ]			
H $\beta$ <sub>Gaussian-fit</sub>	78 $\pm$ 25	[OIII]5008	158 $\pm$ 17
H $\beta$ <sub>Case B</sub> <sup>(a)</sup>	66 $\pm$ 8	H $\alpha$	186 $\pm$ 23
MIRI LRS cont. fluxes [nJy]			
LRS <sub>5.0<math>\mu</math>m</sub>	41 $\pm$ 6	LRS <sub>7.8<math>\mu</math>m</sub>	< 40 <sup>(f)</sup>
LRS <sub>6.3<math>\mu</math>m</sub>	46 $\pm$ 7		
NIRSpec R100 line fluxes [10 $^{-20}$ erg s $^{-1}$ cm $^{-2}$ ] <sup>(b)</sup>			
[OII]3727,3730	46.7 $\pm$ 9.1	H $\gamma$	< 29 <sup>(f)</sup>
[NeIII]3870	32.4 $\pm$ 9.1		
NIRCam band fluxes [nJy] <sup>(c)</sup>			
F115W	< 8.9	F300M	44 $\pm$ 4
F140M	36 $\pm$ 7	F335M	47 $\pm$ 4
F150W	48 $\pm$ 3	F356W	40 $\pm$ 2
F162M	65 $\pm$ 6	F360M	40 $\pm$ 3
F182M	50 $\pm$ 5	F410M	48 $\pm$ 3
F200W	50 $\pm$ 3	F430M	45 $\pm$ 7
F210M	54 $\pm$ 5	F444W	49 $\pm$ 3
F250M	50 $\pm$ 6	F460M	41 $\pm$ 9
F277W	48 $\pm$ 2	F480M	55 $\pm$ 8
ALMA line and continuum fluxes <sup>(d)</sup>			
[OIII]88 $\mu$ m			< 17 $\times$ 10 $^{-20}$ erg s $^{-1}$ cm $^{-2}$ <sup>(f)</sup>
Band 7 cont.			< 28.8 $\mu$ Jy <sup>(f)</sup>

**Notes.** <sup>(a)</sup> H $\beta$  is derived from the H $\alpha$  assuming H $\alpha$ /H $\beta$  = 2.80. <sup>(b)</sup> NIRSpec fluxes are from the UNCOVER DR4 ([Bezanson et al. 2024](#)). <sup>(c)</sup> NIRCam fluxes are from the SUPER catalog of the UNCOVER DR3 ([Suess et al. 2024](#)). <sup>(d)</sup> ALMA fluxes are from [Algera et al. \(2025\)](#). <sup>(f)</sup>  $3\sigma$  upper-limits. All emission line and continuum fluxes are scaled to NIRCam photometry following the description of Section 2.2.

We generate a synthetic filter in the spectral range 4.85–5.30  $\mu$ m, common to both NIRSpec and MIRI LRS, and then normalize MIRI LRS to NIRSpec. We obtain a factor of  $1.24 \pm 0.27$ . Despite the relatively large uncertainty, we renormalize the MIRI LRS spectrum by this factor to have all spectroscopic measurements (e.g. continuum and lines) in the NIRCam photometric scale.

This work only uses the relative uncertainties associated with the specific observations. The additional absolute uncertainty due to the current calibration of the NIRCam, NIRSpec and MIRI absolute spectrophotometry is not taken into account. In general, this is estimated to be at the 1-2%, 15% and 3-8% level<sup>3</sup>, respectively.

## 3. Analysis

### 3.1. MIRI LRS emission line and continuum fluxes

Figure 1 shows the MIRI LRS 2D detector image and the 1D extracted spectrum of U26185 galaxy. The H $\beta$ +[OIII] complex and H $\alpha$  emission line are detected with integrated signal-to-noise (SNR) of 10 and 8, respectively. A faint continuum emission is detected at 5.0 and 6.3  $\mu$ m, with a SNR of 6-7, when multiple spectral elements are stacked. At 7.8  $\mu$ m, where there is no significant detection above  $3\sigma$ , a strong upper-limit is estimated.

MIRI LRS 1D spectrum has a resolving power ranging from 40 to 100 (i.e. FWHMs of 7500 - 3000 km/s) at wavelengths between 5 and 8  $\mu$ m ([Kendrew et al. 2015](#)), respectively. At these

<sup>3</sup> Additional information on the absolute flux calibrations in the JWST instruments: <https://jwst-docs.stsci.edu/jwst-calibration-status>

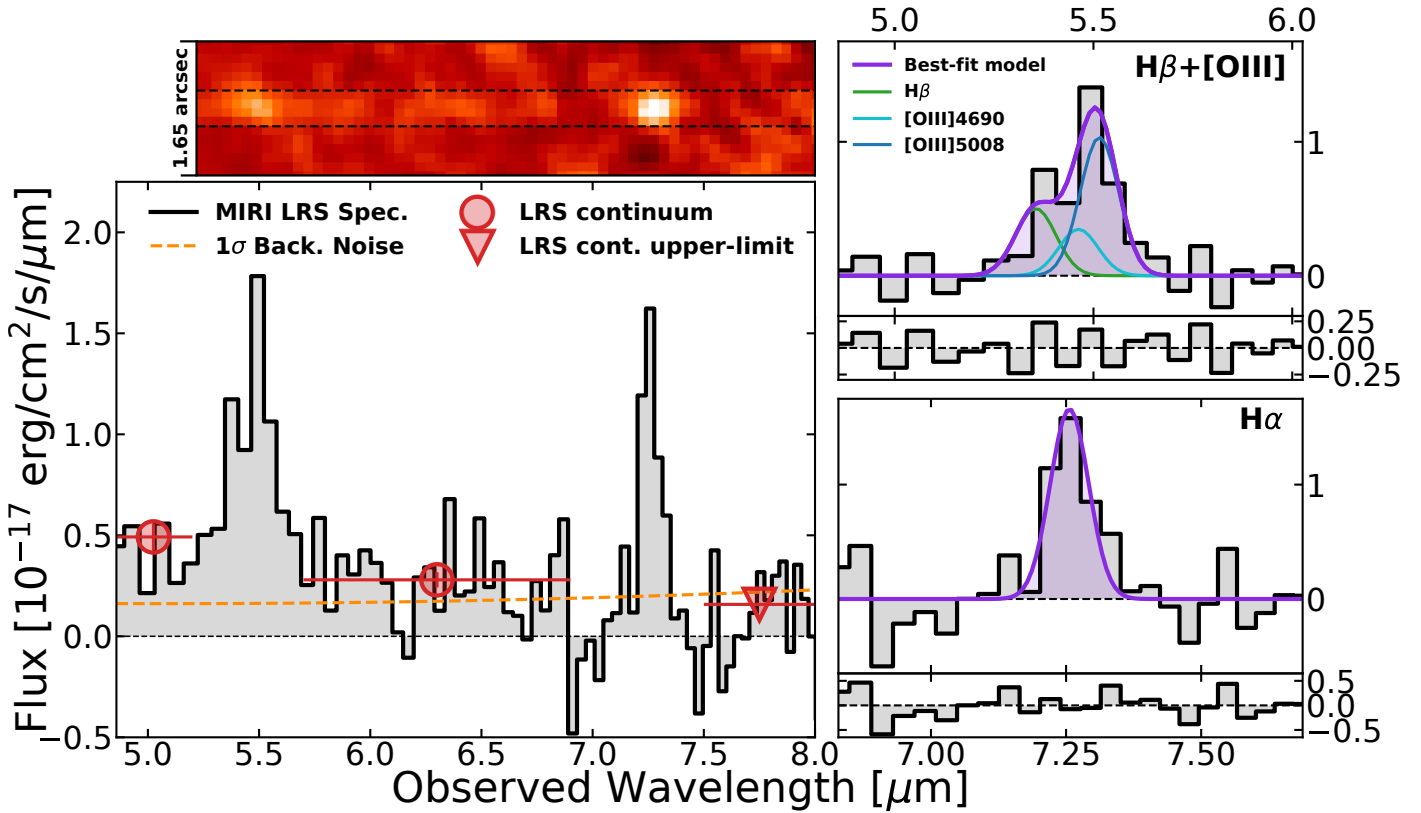


**Fig. 1.** MIRI LRS spectrum and emission line fitting of U28165 galaxy at a redshift of  $10.054 \pm 0.011$ . Upper left panel: area of the MIRI LRS 2D detector combined image with a total exposure time of 13.9 hours. The dashed black lines define the aperture of 0.44 arcsec used to extract the 1D spectrum. Bottom left panel: MIRI LRS 1D extracted spectrum and continuum fluxes. Black and gray area: 1D extracted spectrum showing the detection of the  $\text{H}\beta + [\text{OIII}]$  complex and the  $\text{H}\alpha$  emission line. Red dots and triangle: stacked MIRI LRS continuum fluxes and  $3\sigma$  upper-limit at 5.0, 6.3, and 7.8  $\mu\text{m}$ . Orange dashed line:  $1\sigma$  error of the MIRI LRS spectrum. Upper right panel: three-component Gaussian fit of the  $\text{H}\beta + [\text{OIII}]$  complex (purple line and area). Green, cyan, and blue lines represent the  $\text{H}\beta$ ,  $[\text{OIII}]4960\text{\AA}$ , and  $[\text{OIII}]5008\text{\AA}$ , respectively. Bottom right panel: one-component Gaussian fit of  $\text{H}\alpha$  (purple line and area). Bottom panels of right panels are the residual of the line fitting.

spectral resolutions, the  $\text{H}\beta + [\text{OIII}]$  complex is spectrally unresolved, and all emission lines, including  $\text{H}\alpha$ , are also kinematically unresolved. We perform a three and one-component Gaussian fit to calculate the emission line fluxes and redshift of  $\text{H}\beta + [\text{OIII}]$  and  $\text{H}\alpha$ , respectively. We assume: (i) all emission lines to be unresolved fixing the FWHM to the corresponding spectral resolution of the instrument, (ii) independent redshift for each set of lines as uncertainties on the wavelengths are on average  $\pm 20$  nm, and larger at 5  $\mu\text{m}$  where the  $\text{H}\beta + [\text{OIII}]$  complex is located (see also [Zavala et al. 2025](#)), (iii) the theoretical value of 2.98 for the  $[\text{OIII}]$  line ratio ( $[\text{OIII}]\lambda 5008\text{\AA}/[\text{OIII}]\lambda 4960\text{\AA}$ ; [Storey & Zeippen 2000](#)), and (iv) an one-order polynomial function for the dependency of the continuum on wavelength. The uncertainties on the best-fit parameters, such as flux and redshift, are obtained as the standard deviation of all the individual measurements of 1000 bootstrapped spectra after adding a random Gaussian noise equal to the RMS of the original spectrum. The Gaussian fits are presented in the right panels of Figure 1, while the  $\text{H}\beta$ ,  $[\text{OIII}]\lambda 5008\text{\AA}$ , and  $\text{H}\alpha$  emission line fluxes are given in Table 1. We provide two  $\text{H}\beta$  flux estimates: one obtained directly from the fit to the  $\text{H}\beta + [\text{OIII}]$  complex, and another inferred from the  $\text{H}\alpha$  line assuming Case B recombination ( $\text{H}\alpha/\text{H}\beta = 2.8$ ; for  $T_e = 15000$  K and  $n_e = 1000 \text{ cm}^{-3}$ ). Both  $\text{H}\beta$  fluxes are consistent within uncertainties (see Section 4.1 for additional details).

We derive a redshift equal to  $z = 10.010 \pm 0.020$  and  $z = 10.054 \pm 0.011$  for the  $\text{H}\beta + [\text{OIII}]$  complex and the  $\text{H}\alpha$  line, respectively. The  $\text{H}\beta + [\text{OIII}]$  redshift is less reliable due to the

larger uncertainties in the LRS wavelength calibration around 5  $\mu\text{m}$  and because the lines are spectrally unresolved. We therefore consider the  $\text{H}\alpha$ -based value as the fiducial redshift of U26185 and adopt it for all subsequent analysis. The  $\text{H}\alpha$ -based redshift is in agreement within uncertainties with the NIRSpec-based redshift value ( $z = 10.061^{+0.011}_{-0.013}$ ).

We also calculate the continuum emission at 5.0, 6.3, and 7.8  $\mu\text{m}$  by stacking multiple spectral elements. We define three spectral windows clean of emission lines: 4.85 - 5.2  $\mu\text{m}$ , 5.7 - 6.9  $\mu\text{m}$ , and 7.5 - 8  $\mu\text{m}$ . We obtain fluxes of  $41 \pm 6$  and  $46 \pm 7$  nJy at 5.0 and 6.3  $\mu\text{m}$ , and a  $3\sigma$  upper-limit of 40 nJy at 7.8  $\mu\text{m}$ . Values are given in Table 1 and represented in Figure 1.

We combine the measured emission-line fluxes with the stacked continuum measurements to derive the equivalent widths (EWs) of  $\text{H}\beta$ ,  $[\text{OIII}]\lambda\lambda 4960, 5008\text{\AA}$ , and  $\text{H}\alpha$  emission lines. The continuum flux density underlying each line is estimated by fitting a linear relation to the two MIRI continuum fluxes and extrapolating to the wavelength of each line. The EWs are then computed as the ratio of the line flux to the corresponding continuum flux density. The resulting values are reported in Table 2.

### 3.2. SED-fitting analysis

We perform a SED fitting analysis using the SpectroPhotometric version of CIGALE ([Boquien et al. 2019](#); [Burgarella et al. 2025](#)), and the combination of NIRCam photometry, NIRSpec spectrum, and MIRI LRS and ALMA emission lines and con-

tinuum fluxes (see Table 1). NIRCam wide- and medium-band filters, together with synthetic continuum bands derived from MIRI LRS, probe the rest-frame UV to optical wavelengths up to  $0.7\,\mu\text{m}$ , while ALMA provides access to the rest-frame far-IR continuum at  $90\,\mu\text{m}$ . NIRSpec spectra cover the rest-frame UV up to  $0.45\,\mu\text{m}$ , revealing both the continuum and lines, including  $\text{CIII}\lambda 1909\text{\AA}$ ,  $[\text{OII}]\lambda\lambda 3727,3730\text{\AA}$  and  $[\text{NeIII}]\lambda 3870\text{\AA}$ . In addition to the continuum fluxes, MIRI LRS provides the  $[\text{OIII}]\lambda 5008\text{\AA}$  and  $\text{H}\alpha$ , while ALMA provides the  $[\text{OIII}] 88\,\mu\text{m}$  emission line fluxes. Altogether, this constitutes one of the most comprehensive multiwavelength datasets available for a galaxy at  $z \sim 10$ , simultaneously constraining the continuum and lines from the rest-frame UV to the FIR (see also Zavala et al. 2024; Carniani et al. 2024a; Castellano et al. 2025b).

The SFH is modeled as the combination of a delayed- $\tau$  component, representing the bulk of the stellar mass, and a constant star-formation burst accounting for the young stellar population. The delayed- $\tau$  component is characterized by e-folding times ( $\tau$ ) ranging from 1 to 250 Myr and ages between 25 and 200 Myr. The constant young burst spans ages from 1 to 10 Myr. We adopted the stellar population models from Bruzual & Charlot (2003) and the Chabrier (2003) IMF. We included nebular continuum and lines, using an electron density of  $1000\,\text{cm}^{-3}$  following the electron density-redshift relation derived for high- $z$  galaxies up to  $z \sim 10$  (Abdurro'uf et al. 2024), ionised parameter,  $\log(U)$ , values from  $-3.2$  to  $-2.0$ , and the fraction of Lyman continuum photons escaping the galaxy set to zero. Both stellar populations and nebular emission use metallicities ranging from 2% to 20%  $Z_\odot$ .

Dust attenuation is modeled using the module of CIGALE (dustatt\_modifed\_starburst). Stellar attenuation follows the modified Calzetti prescription of Noll et al. (2009), based on the Calzetti law (Calzetti et al. 2000). We vary the attenuation curve slope  $\delta$  between 0 and  $-0.6$ , and fix the UV bump amplitude to zero. Nebular dust attenuation is modeled using the Small Magellanic Cloud (SMC) extinction curve (Pei 1992). The visible nebular dust attenuation ranges from 0 to 0.4 mag, as derived from the Balmer decrements (see Section 4.1), and the stellar-to-nebular dust attenuation ratio goes from 0.33 to 1. This configuration provides the flexibility to explore dust attenuation curves steeper than the Calzetti law, as commonly observed in galaxies with low stellar masses and metallicities (e.g. Álvarez-Márquez et al. 2019; Shvai et al. 2020; Fudamoto et al. 2020). Infrared emission is modeled using the dust templates of Draine & Li (2007), with parameters fixed to those derived for the average population of high- $z$  ALPINE galaxies (Burgarella et al. 2022).

The results of the CIGALE Bayesian analysis are presented in Table 2, while the best-fit SED model is shown in Figure 2. Assuming a two-component SFH, we derive a total stellar mass of  $(1.7 \pm 0.3) \times 10^8\,M_\odot$  and a mass-weighted stellar age of  $65 \pm 20$  Myr. The ongoing burst, with an age of  $7 \pm 3$  Myr, is characterized by a star formation rate (SFR) of  $1.7 \pm 0.4\,M_\odot\,\text{yr}^{-1}$  and stellar mass of  $(1.7 \pm 0.4) \times 10^7\,M_\odot$ , i.e. 10% of the stellar mass of the galaxy. The Balmer break strength (D4000; Balogh et al. 1999), defined as the ratio of the flux in the red continuum to that in the blue continuum, is  $1.33 \pm 0.03$  supporting the presence of a more mature stellar population. The inferred dust attenuation favors a curve steeper than the standard Calzetti law, with a  $\delta = -0.3 \pm 0.2$  and a  $A_V = 0.20 \pm 0.09$  mag. The nebular metallicity is constrained to  $0.05 \pm 0.01\,Z_\odot$ , with an ionization parameter of  $\log(U) = -2.6 \pm 0.2$ . While the  $A_V$  values derived independently from emission lines and SED fitting are consistent within the uncertainties (see Section 4.1), the fit is affected

**Table 2.** Intrinsic, de-lensed physical properties of U26185 assuming a star-forming galaxy scenario.

Properties derived from emission lines and continuum		
Redshift		$10.054 \pm 0.011$
$M_{\text{UV}}$	[mag]	$-18.83 \pm 0.07$
$A_{V\text{-lines}}$	[mag]	$0.0_{-0.0}^{+0.4}$
$\text{SFR}_{\text{H}\alpha}$	$[M_\odot\,\text{yr}^{-1}]$	$1.3 \pm 0.2$
$\log(\xi_{\text{ion}})$	$[\text{Hz}\,\text{erg}^{-1}]$	$25.50 \pm 0.06$
$\text{EW}(\text{H}\beta)$	[Å]	$138 \pm 26$
$\text{EW}([\text{OIII}]4960,5008)$	[Å]	$467 \pm 81$
$\text{EW}(\text{H}\alpha)$	[Å]	$1399 \pm 271$
$\log(U)$		$-2.5 \pm 0.1$
Metallicity	$[Z_\odot]$	$0.04 \pm 0.01$
Properties derived from SED-fitting analysis		
$A_{V\text{-SED}}$	[mag]	$0.20 \pm 0.09$
$\beta_{\text{UV}}$		$-2.29 \pm 0.06$
$\text{SFR}_{\text{SED}-10\,\text{Myr}}$	$[M_\odot\,\text{yr}^{-1}]$	$1.7 \pm 0.4$
$M_{\text{Stellar}}$	$[\times 10^8\,M_\odot]$	$1.7 \pm 0.3$
Mass weighted Age	[Myr]	$65 \pm 20$
$\text{sSFR}$	$[\text{Gyr}^{-1}]$	$7.6 \pm 1.2$
$M_{\text{Stellar-burst}}$	$[\times 10^8\,M_\odot]$	$0.17 \pm 0.04$
$\text{Age}_{\text{burst}}$	[Myr]	$7 \pm 3$
D4000		$1.33 \pm 0.03$
$\log(U)$		$-2.6 \pm 0.2$
Metallicity	$[Z_\odot]$	$0.05 \pm 0.01$

by limitations in the nebular model grid at very low metallicities ( $< 0.05\,Z_\odot$ ). In particular, for U26185 the observed  $[\text{OIII}]\lambda 5008$ -to- $\text{H}\alpha$  line ratio of  $\sim 0.85$  implies a metallicity below  $0.05\,Z_\odot$  according to the nebular models implemented in CIGALE. As the available models do not have a grid to fully reproduce such low-metallicity line ratios, the fitting procedure could compensate by invoking differential dust attenuation between the two lines (e.g., a steeper attenuation slope or higher overall dust attenuation), or may even fail to reproduce within  $1\sigma$  the observed line fluxes of  $\text{H}\alpha$  (see Figure 2). This degeneracy may lead to a modest overestimation of the total dust attenuation and, consequently, affect the inferred metallicity. Nevertheless, the combined continuum and line model provides a good match to the MIRI LRS spectrum (see the left panel of Figure 2), and the dust attenuation and metallicity are in agreement with the ones derived using only emission lines (see Table 2).

## 4. Results

### 4.1. Dust attenuation

We estimate the nebular dust attenuation using Balmer decrements derived from the hydrogen recombination lines covered by the combined MIRI LRS and NIRSpec observations. The observed  $\text{H}\alpha/\text{H}\beta$ ,  $\text{H}\alpha/\text{H}\gamma$ , and  $\text{H}\beta/\text{H}\gamma$  line ratios are  $2.4 \pm 0.8$ ,  $> 6.4$ , and  $> 2.69$ , respectively. Within the uncertainties, these Balmer decrements are consistent with the Case B recombination values expected for ISM inferred in previously observed  $z > 10$  galaxies (e.g.,  $T_e = 15,000\,\text{K}$  and  $n_e = 1000\,\text{cm}^{-3}$ ; Hsiao et al. 2024b; Abdurro'uf et al. 2024; Álvarez-Márquez et al. 2025):  $\text{H}\alpha/\text{H}\beta = 2.80$ ,  $\text{H}\alpha/\text{H}\gamma = 5.93$ , and  $\text{H}\beta/\text{H}\gamma = 2.12$ . Considering Cardelli et al. (1989), these results are compatible with no dust attenuation, but the  $1\sigma$  uncertainty in the  $\text{H}\alpha/\text{H}\beta$  provides an upper-limit of 0.4 mag ( $A_{V\text{-lines}} = 0_{-0.0}^{+0.4}$  mag).

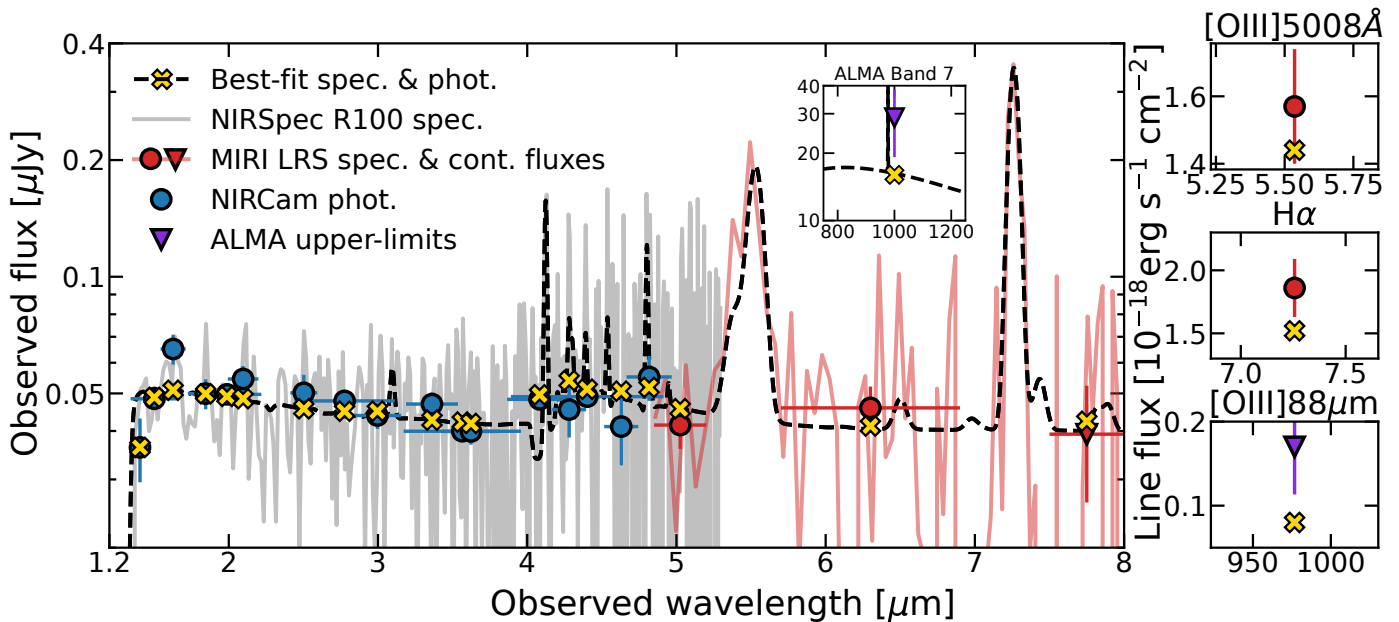


**Fig. 2.** SED-fitting analysis using the magnified, scaled fluxes of all detected lines and continuum emission of U26185 at redshift of 10.05. The analysis combine the NIRCam photometry (Blue dots), NIRSpec R100 spectrum (gray line), MIRI LRS derived continuum photometry and  $[\text{OIII}]\lambda 5008\text{\AA}$  and  $\text{H}\alpha$  fluxes (Red dots for detections and red triangles for  $3\sigma$  upper-limits), and the ALMA Band 7 continuum and  $[\text{OIII}]\lambda 88\mu\text{m}$   $3\sigma$  upper-limits (Purple triangles). The best-fit CIGALE model is represented with dashed back line, and its synthetic NIRCam photometry, and MIRI LRS and ALMA continuum fluxes and emission lines fluxes are represented by yellow crosses.

CIGALE SED-fitting analysis, combining rest-frame UV-optical spectra, emission lines, and photometry together with the ALMA continuum upper-limits, provides an absolute (nebular + stellar) visible dust attenuation of  $\text{Av-SED} = 0.20 \pm 0.09$  mag. These values are consistent, within uncertainties, with those derived from Bagpipes SED-fitting analysis combining only NIRSpec spectra and NIRCam wide-band photometry ( $\text{Av-SED} = 0.08^{+0.08}_{-0.05}$  mag; [Goulding et al. 2023](#)). However, we note that the CIGALE analysis could be slightly overestimating the dust attenuation, even though the current  $\text{A}_V$  values derived from emission lines and SED-fitting are still consistent within uncertainties (see Section 3.2), and lower than the measured nebular upper-limit. Additionally, the current dust attenuation value of CIGALE is in agreement with the upper-limit measured in the dust continuum emission at  $90\mu\text{m}$  (see Figure 2).

Recent deep ALMA Band 7 observations have placed a  $3\sigma$  upper-limit of  $5.5 \times 10^5 \text{ M}_\odot$  to the cold dust mass present in U26185 ([Algera et al. 2025](#)). This upper-limit represents a small dust-to-stellar mass ratio ( $\text{M}_{\text{dust}}/\text{M}_{\text{stellar}} < 3.2 \times 10^{-3}$ ), suggesting very low or negligible dust content in this galaxy, and compatible with no attenuation as derived from the optical emission lines and SED-fitting analysis. Therefore, we assume an  $\text{A}_V = 0$  mag throughout this paper, and a  $\text{H}\beta$  flux derived assuming Case B recombination and the  $\text{H}\alpha$  flux ( $\text{H}\beta_{\text{Case B}}$ ; see Table 1).

#### 4.2. Star-formation history and ionizing photon production efficiency

The instantaneous SFR derived from the total  $\text{H}\alpha$  luminosity and considering no-dust attenuation,  $\text{SFR}_{\text{H}\alpha}$ , is  $1.4 \pm 0.2$  and  $1.3 \pm 0.2 \text{ M}_\odot \text{ yr}^{-1}$  using the relations by [Theios et al. \(2019\)](#) and [Reddy et al. \(2022\)](#), calibrated for galaxies with metallicities of  $0.1 \text{ Z}_\odot$  and  $0.05 \text{ Z}_\odot$ , respectively. These values are consistent within  $1\sigma$  uncertainties with those obtained from SED-fitting

analyses using CIGALE ( $\text{SFR}_{\text{SED-10 Myr}} = 1.7 \pm 0.4 \text{ M}_\odot \text{ yr}^{-1}$ ) and Bagpipes  $\text{SFR} = 1.25^{+0.18}_{-0.20} \text{ M}_\odot \text{ yr}^{-1}$ ; [Goulding et al. 2023](#)) both averaged over the last 10 Myr. Additionally, the SFR derived from the UV luminosity ( $\text{SFR}_{\text{UV}}$ ) average over the past 100 Myr, is  $1.0 \text{ M}_\odot \text{ yr}^{-1}$ . We assume a metallicity of  $0.1 \text{ Z}_\odot$  ([Theios et al. 2019](#)) and a UV luminosity density of  $1.5 \times 10^{28} \text{ erg s}^{-1} \text{ Hz}^{-1}$  at  $1500\text{\AA}$ , computed from the average fluxes of the F150W and F200W NIRCam bands.

The resulting burstiness parameter (SFR $_{\text{H}\alpha}$ -to-SFR $_{\text{UV}}$  ratio) is  $1.4 \pm 0.2$  for a metallicity of  $0.1 \text{ Z}_\odot$ , where SFR $_{\text{H}\alpha}$  and SFR $_{\text{UV}}$  trace star formation over 10 Myr and 100 Myr timescales, respectively, assuming constant SFH. The different timescales probed by these SFR indicators allow us to investigate the burstiness of the star formation. The inferred burstiness parameter consistent with unity in  $2\sigma$ , indicating that the galaxy is not dominated by a recent strong burst. This is consistent with the SFH derived from CIGALE, which suggests that the stellar population has a mass-weighted age of  $65 \pm 20$  Myr, also consistent with the half-mass ages derived from Bagpipes ( $65^{+31}_{-20}$  Myr; [Goulding et al. 2023](#)). This is also supported by the Balmer break strength higher than 1, indicating that a more mature stellar population should be invoked. Although the error makes the measurement in full agreement with unity, the slightly elevated value than 1 (1.4) suggests the presence of an additional young stellar population coexisting with the bulk of the stellar component, in agreement with the young burst identified by CIGALE, which contributes  $\sim 10\%$  of the total stellar mass.

Following the methodology outlined by [Álvarez-Márquez et al. \(2024\)](#), we derive an ionizing photon production efficiency of  $\log(\xi_{\text{ion}} [\text{Hz erg}^{-1}]) = 25.50 \pm 0.06$  under the assumption of zero LyC escape fraction and non-dust attenuation. This value is higher than the commonly adopted canonical value of  $25.2 \pm 0.1 \text{ Hz erg}^{-1}$  ([Robertson et al. 2023](#)), yet remains consistent with values inferred from the redshift extrapolation of intermediate-redshift galaxies ([Matthee et al. 2017](#); see also Fig-

ure 3 of Álvarez-Márquez et al. (2024). The inferred  $\log(\xi_{\text{ion}})$  is typical of sources in the epoch of reionization (e.g., Atek et al. 2024; Fujimoto et al. 2023; Tang et al. 2023; Morishita et al. 2023; Rinaldi et al. 2024; Álvarez-Márquez et al. 2024; Morishita et al. 2024; Simmonds et al. 2024; Komarova et al. 2025; Llerena et al. 2025; Prieto-Jiménez et al. 2025; Zavala et al. 2025), and of galaxies at intermediate redshifts ( $2 < z < 5$ ) exhibiting the highest specific star-formation rates,  $\log(\text{sSFR}[\text{yr}^{-1}]) \sim -7.5$  (Castellano et al. 2023a), similar ones than that of U26185 ( $\log(\text{sSFR}[\text{yr}^{-1}]) \sim -7.6 \pm 1.2$ ). In the context of galaxies at  $z > 10$ , U26185 exhibits an intermediate  $\xi_{\text{ion}}$  compared to GHZ2 ( $25.7^{+0.2}_{-0.1} \text{ Hz erg}^{-1}$ , Calabró et al. 2024), GN-z11 ( $25.66 \pm 0.06 \text{ Hz erg}^{-1}$ , Álvarez-Márquez et al. 2025), and MACS0647-JD and JADES-GS-z14-0 ( $25.3 \pm 0.1 \text{ Hz erg}^{-1}$ , Hsiao et al. 2024b; Helton et al. 2025).

U26185 is also characterized by a very high  $\text{H}\alpha$  equivalent width,  $\text{EW}(\text{H}\alpha) = 1399 \pm 271 \text{ \AA}$ . This value is consistent with the extrapolation of the  $\text{EW}(\text{H}\alpha) \propto (1+z)^{2.1}$  relation derived from a combination of pre-JWST measurements and the results of the JADES and MIDIS JWST surveys (Rinaldi et al. 2023; see also Figure 4 of Álvarez-Márquez et al. 2024). Binary Population and Spectral Synthesis (BPASS; Eldridge & Stanway 2020) models indicate that  $\text{EW}(\text{H}\alpha)$  values exceeding  $1000 \text{ \AA}$  can only be produced by stellar populations younger than 10 Myr. Additionally, ionizing photon production efficiencies of  $\log(\xi_{\text{ion}}) \gtrsim 25.5 \text{ Hz erg}^{-1}$  require young, massive star-forming bursts with stellar masses of at least  $\sim 10^7 M_{\odot}$ , owing to the stochastic nature of massive star formation (Stanway & Eldridge 2023). Furthermore, the location of U26185 in the  $\log(\xi_{\text{ion}})$ – $\text{EW}(\text{H}\alpha)$  plane (see Figure 5 of Prieto-Jiménez et al. 2025) suggests stellar population ages of  $\sim 4$ –6 Myr, for an instantaneous burst. All these independent constraints, together with the slightly elevated value relative to unity of the burstiness parameter, are consistent with the star-forming burst inferred from CIGALE, which indicates the presence of a young stellar component with an age of  $7 \pm 3$  Myr and a stellar mass of  $(1.7 \pm 0.4) \times 10^7 M_{\odot}$ .

In summary, the galaxy U26185 is characterized by a SFH that can be decomposed into two distinct stellar populations. The dominant, more mature component—which contains the bulk of the stellar mass—has a mass-weighted age of  $65 \pm 20$  Myr and a stellar mass of  $(1.5 \pm 0.3) \times 10^8 M_{\odot}$ , indicating that the majority of the galaxy’s stars formed around redshift  $z \sim 11$ . The young stellar population contributes  $\sim 10\%$  of the total stellar mass, with a mass of  $(1.7 \pm 0.4) \times 10^7 M_{\odot}$  and an age of  $7 \pm 3$  Myr. The ongoing burst is characterized by a star-formation rate of  $1.3 \pm 0.2 M_{\odot} \text{ yr}^{-1}$ , assuming a metallicity of  $0.05 Z_{\odot}$ .

#### 4.3. Ionization and emission line ratios

We combine the MIRI LRS and NIRSpec R100 line fluxes (see Table 1) to derive the following emission line ratios, which are then used in the diagnostic diagrams:

$$\begin{aligned} R2 &= [\text{O II}]3727, 3730 \text{ \AA} / \text{H}\beta \\ R3 &= [\text{O III}]5008 \text{ \AA} / \text{H}\beta \\ R23 &= ([\text{O III}]5008 \text{ \AA} + [\text{O II}]3727, 3730 \text{ \AA}) / \text{H}\beta \\ O32 &= [\text{O III}]4960, 5008 \text{ \AA} / [\text{O II}]3727, 3730 \text{ \AA} \\ \text{Ne3O2} &= [\text{Ne III}]3870 \text{ \AA} / [\text{O II}]3727, 3730 \text{ \AA} \\ \hat{R} &= 0.47 \times R2 + 0.88 \times R3 \end{aligned}$$

where  $\text{H}\beta$  is derived assuming  $\text{H}\alpha/\text{H}\beta = 2.80$  (see § 3.1). The line ratios along with their associated uncertainties, are listed on Table 3.

We use the combination of these line ratios to investigate the nature of the ionization source in U26185. Figure 3 displays, as a red star, the position of U26185 in these diagnostic diagrams. For comparison, we also include data (colored squares) for  $z > 9$  galaxies (MACS1149-JD1, Stiavelli et al. 2023; RXJ2129-z95, Williams et al. 2023; MACS0647-JD, Hsiao et al. 2023; GN-z9p3, Boyett et al. 2023; GN-z9p4, Schaerer et al. 2024; GHz2, Castellano et al. 2024; Zavala et al. 2025; GS-z9-0, Curti et al. 2025; GN-z11, Bunker et al. 2023; Álvarez-Márquez et al. 2025; GS-z14-0, Helton et al. 2025; EGS-25297, Donnan et al. 2025; GN-55757, GN-3990, GS-265801, EGS-87132, UDS-22431, UDS-833482, U-13151 and U-3686, Pollock et al. 2025 and references therein) and other  $z > 5$  N-rich galaxies (colored circles: CEERS-1019, Larson et al. 2023; Zamora et al. 2025; GS-3073, Ji et al. 2024; RXCJ2248-ID, Topping et al. 2024). Blue and red markers display a sample of  $z > 3$  star-forming and AGN galaxies, respectively, obtained from JWST surveys (JADES, Cameron et al. 2023; Bunker et al. 2024; Curti et al. 2024; CEERS, Sanders et al. 2024; ERO+GLASS+CEERS, Nakajima et al. 2023). Colored diamonds represent the stacked value for the  $z > 5$  subsamples drawn from the 500 high redshift galaxies presented in Roberts-Borsani et al. (2024). In addition, we include a sample of local metal-poor galaxies (gray circles, Izotov et al. 2006) and the CLOUDY photoionization models for SFGs and AGN as presented in Calabró et al. (2023) and Calabró et al. (2024).

U26185 appears as an outlier from the population of high- $z$  star-forming and AGN galaxies, presenting the lowest R3, O32 and R23 observed ratios up to date (see Figure 3). U26185 also clearly deviates from the ratios observed in local metal-poor galaxies. The line ratios in U26185 are compatible with low ionization parameter ( $\log(U) \sim -2.5$ ) and metal-poor ( $12+\log(\text{O/H}) \sim 7.5$ ) CLOUDY photoionization models of SFGs. This low ionization parameter is also consistent with the value independently derived by other tracers. We derive ionization parameters  $\log(U)$  of  $-2.5 \pm 0.1$  and  $-2.4 \pm 0.1$  based on the O32 –  $\log(U)$  relations from Díaz et al. (2000), derived using single-star photoionization models, and Papovich et al. (2022) for local and  $1 < z < 2$  galaxies, respectively. These values are also in agreement with the results obtained from CIGALE (Table 2). If we consider the AGN CLOUDY models, the line ratios would predict a larger ionization parameter ( $\log(U) \sim -2$ ) and a higher metallicity ( $12+\log(\text{O/H}) \sim 8.1$ ). See next Section for metallicity estimates and discussions.

#### 4.4. Metallicity

The dependence of the optical line ratios with the metallicity has been studied in detail using the  $T_e$ -direct method and large samples of galaxies at redshifts up to 10. In this work, we use some of the most recent studies to infer the metallicity based on these optical line ratios (see Section 4.3). Concretely, we consider the Sanders et al. (2025) and Chakraborty et al. (2025) relations (henceforth, S+25 and C+25, respectively) derived from high- $z$  ( $2 < z < 10$ ) sample of galaxies with metallicities in the range of  $12+\log(\text{O/H}) \sim 7.2$ –8.6 observed with JWST. For completeness, we also consider the relations from Nakajima et al. (2022) (henceforth, N+22), derived from a SDSS sample of local galaxies covering a wider metallicity range ( $12+\log(\text{O/H}) \sim 6.9$ –8.9). Figure 4 displays the empirical relations presented in N+22, S+25 and C+25 for each line ratio as dotted, solid and dashed

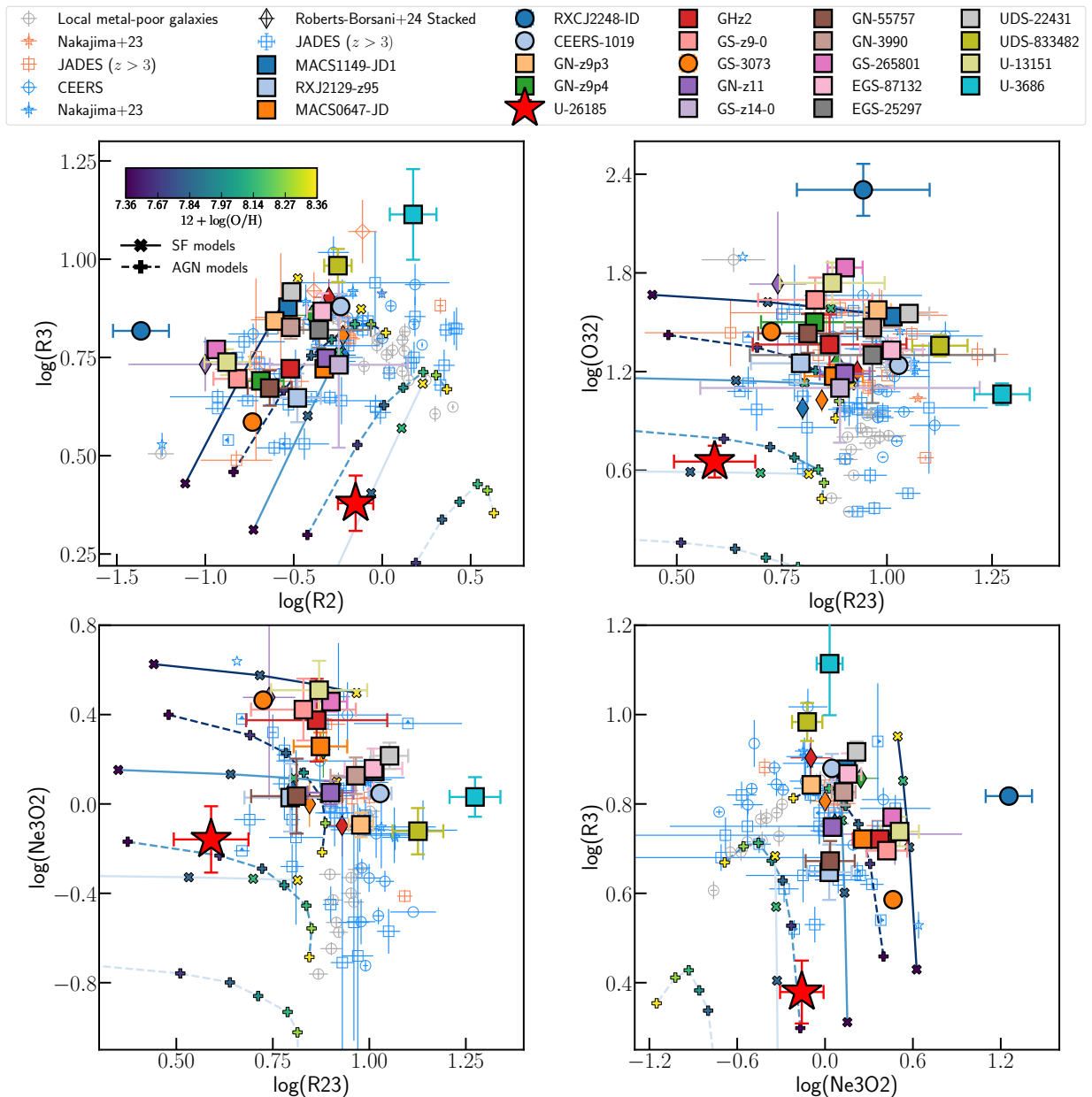


**Fig. 3.** Line ratio diagnostic diagrams. Red star and colored squares and circles represent U26185 and the high-z and N-rich samples, as presented in Sect. 4.3. Gray, blue and red points display a sample of local metal-poor galaxies (Izotov et al. 2006) and high-z SF and AGN galaxies from the main JWST surveys (Sect. 4.3 for further details), respectively. Colored squares and circles represent recent JWST-observed  $z > 9$  galaxies and  $z > 5$  N-rich galaxies, respectively. Blue, orange, red, green and purple diamonds display the stacked values for the  $z > [5, 6, 7, 8, 9]$  galaxy subsamples from Roberts-Borsani et al. (2024), respectively. Solid and dashed lines represent the CLOUDY photo-ionization models presented in Calabro et al. (2023) for the AGN and SF scenarios, respectively. Increasingly darker blue lines represent an increasing  $\log(U) = [-3, -2.5, -2]$  values while the metallicities are displayed as colored markers.

lines, respectively. Gray points represent general samples of local metal-poor galaxies (Izotov et al. 2006), and  $z > 3$  galaxies from CEERS (Sanders et al. 2025), JADES (Bunker et al. 2023; Cameron et al. 2023) and ERO+GLASS+CEERS (Nakajima et al. 2023). For comparison, we included the high-z and N-rich galaxies as presented in Figure 3. Red horizontal line and shaded area represent the line ratio values and uncertainties for U26185, respectively. Table 3 summarizes the U26185 metallicities derived from the empirical relations presented in S+25, C+25 and N+22. In addition to the values derived from the general samples, we include the metallicities obtained from the medium  $\text{EW}(\text{H}\beta)$  bin (i.e.,  $100 < \text{EW}(\text{H}\beta) [\text{\AA}] < 200$ ) in N+22, to

explore potential dependence on  $\text{EW}(\text{H}\beta)$ . The metallicity values derived from  $\text{R}_2$ ,  $\text{R}_{23}$  and  $\hat{\text{R}}$  from S+25 and C+25 are obtained by extrapolating their expressions down to  $12+\log(\text{O/H}) = 6.9$ , to match the N+22 metallicity coverage.

Overall, the emission-line ratios of U26185 place this galaxy in the low-metallicity regime, with all diagnostics consistently indicating  $12+\log(\text{O/H}) < 8$ . The  $\text{R}_2$ ,  $\text{R}_{23}$ ,  $\text{O}_{32}$ , and  $\text{Ne}_{3O2}$  indicators are strongly dependent on the ionization conditions, whereas the  $\text{R}_{23}$  diagnostic provides the most robust metallicity estimate, with an intrinsic scatter of 0.14 dex and a weaker dependence on ionization parameters (Nakajima et al. 2022; Sanders et al. 2025). We therefore adopt

as our fiducial metallicity the R23-based calibration from N+22 ( $12+\log(\text{O/H})=7.31\pm0.13$ ), corresponding to the medium EW(H $\beta$ ) galaxy sample. This choice is motivated by the fact that U26185 exhibits EW(H $\beta$ ) values within this regime and avoids extrapolation into extremely metal-poor conditions, which would be required when applying the calibrations of S+25 and C+25. We obtain similar metallicities when using the relations derived from local analogs, combining the R23 and O32 ratios to improve the accuracy in the low-metallicity regime ( $12+\log(\text{O/H})=7.3\pm0.4$ ; Izotov et al. 2019). Using the *genesis-metallicity* code (Langeroodi & Hjorth 2024), which is based a non-parametric combination of the emission line ratios, we found  $12+\log(\text{O/H})=7.09\pm0.05$ , fully compatible with the low limit provided by our extrapolations of  $\hat{R}$  for S+25 and C+25.

The adopted metallicity derived from the most reliable R23 line ratio ( $12+\log(\text{O/H})=7.31\pm0.13$ ;  $0.04\pm0.01 \text{ Z}_\odot$ ) is in agreement with the one derived from CIGALE (see Table 2). This metallicity represents the lowest metallicity measured so far in galaxies at redshifts above 9. Concretely, other high- $z$  galaxies such as MACS0647, MACSJ1149-JD1, GHz2 or GNz11 present typical values  $7.4 < 12+\log(\text{O/H}) < 7.9$  (see Figure 4), derived by the  $T_e$ -direct method. These higher metallicities could be explained by the larger stellar mass in these galaxies. In Section 5.2 we will discuss U26185 in the context of the mass-metallicity relation for high- $z$  galaxies.

For completeness, we consider the scenario where the ionization of the nebular emission is produced by an AGN. We use the so-called  $T_e$ -AGN method, which considers a different  $T_e[\text{O}^{++}]-T_e[\text{O}^+]$  relation, to derive the metallicity (Dors et al. 2020a; Dors 2021). Assuming a  $T_e[\text{O}^{++}]=15000 \text{ K}$  and considering that the higher ionized oxygen species represent  $\sim 20\%$  the total O/H abundance in AGNs (Dors et al. 2020b), we derive a metallicity of  $12+\log(\text{O/H})=7.9\pm0.4$ . This value is in agreement with the CLOUDY metallicities of AGNs (see Figure 3).

## 5. Discussion

### 5.1. U26185: no evidence of an elusive X-ray luminous AGN

U26185 has been identified as one of the highest redshift AGNs known so far based on just its detection as a luminous X-ray source (Bogdán et al. 2024). The detection at rest-frame 23-79 keV but not at 11-23 keV is interpreted as due to a heavy absorption of the energy source. Assuming a conservative column density of  $2 \times 10^{24} \text{ cm}^{-2}$ , the X-ray emission is consistent with the presence of a Compton-thick AGN characterized by an intrinsic 2-10 keV luminosity of  $1.9 \times 10^{44} \text{ erg s}^{-1}$ . This luminosity corresponds to a black hole mass of about  $4 \times 10^7 \text{ M}_\odot$  for a X-ray-to-bolometric luminosities ratio of 21 and an Eddington accretion rate (Bogdán et al. 2024). This high X-ray luminosity is similar to that of galaxy GHz9 ( $1.8-3.8 \times 10^{44} \text{ erg s}^{-1}$ ), a galaxy at a redshift of 10.145, recently detected by Chandra and also showing hybrid properties of coexisting star-formation and AGN from the JWST NIRSpec spectrum (Napolitano et al. 2025b; Kovács et al. 2024). The Compton-thick scenario predicts the existence of an obscuring material with a very large column density, and the presence of a luminous AGN. This material can be associated with dust and gas in the host galaxy and/or in a dusty torus around the accreting BH, or with the high density gas in the Broad Line Region (BLR), at distances closer to the BH and accretion disk than the torus. However, as explained below, no trace of internal dust and of a luminous AGN is present in the UV and optical spectrum of U26185 when combining the NIRSpec

and MIRI LRS data. In the following, based on the combination of the NIRSpec and LRS data, we evaluate whether there is an evidence for obscuring dust and for a luminous Compton-thick AGN, or whether the alternative scenario of a lower luminosity AGN should be further considered requiring additional X-ray data.

If U26185 were hosting a classical type 1 AGN, its X-ray luminosity could be derived from the (extinction-corrected) H $\alpha$  luminosity assuming the well known relation with the intrinsic 2-10 keV emission for low- $z$  quasars and type 1 AGNs (Ho et al. 2001; Jin et al. 2012) holds at redshift 10. Following this relation, the derived 2-10 keV luminosity would be in the  $8-11 \times 10^{42} \text{ erg s}^{-1}$  range, conservatively assuming the entire H $\alpha$  luminosity is due to a type 1 AGN. This X-ray luminosity is a factor of at least ten lower than the estimated from the X-ray flux under the scenario of a Compton-thick type 1 AGN. Our H $\alpha$ -derived X-ray luminosity is even factors  $\sim 2-6$  lower than the 2-10 keV luminosity derived with the alternative lower column density solution (see discussion above and Bogdán et al. 2024).

A standard type 2 AGN could also be invoked as the source of the X-ray emission. A majority (75%) of low- $z$  Seyfert 2 galaxies have column densities above  $10^{23} \text{ cm}^{-2}$ , with half of them having densities higher than  $10^{24} \text{ cm}^{-2}$  (Risaliti et al. 1999), similar to those derived for U26185 (Bogdán et al. 2024). However, although with some scatter, the median 2-10 keV-to-H $\alpha$  luminosity ratio is about 2 for Seyfert 2 galaxies (Ho et al. 2001) and therefore the H $\alpha$ -derived X-ray luminosity ( $1.2 \times 10^{42} \text{ erg s}^{-1}$ ) would be much lower (factors of 20-40) than the lowest 2-10 keV luminosity estimated from *Chandra* ( $> 2-4 \times 10^{43} \text{ erg s}^{-1}$ , Bogdán et al. 2024). Moreover, the extension of the line-free continuum measurements up to the rest-frame  $0.7 \mu\text{m}$  with the LRS (see Table 1 and Figure 2) does not show any indication of an increased red continuum due to hot-dust emission. That red continuum is present in the spectrum of high- $z$  little red dots (LRDs; e.g. Akins et al. 2025), and has been detected in GN-z11 (Crespo Gómez et al. 2025), a galaxy at redshift 10.6 where the presence of a supermassive BH has been invoked (Maiolino et al. 2024) while the UV-optical spectrum appears to be dominated by a nuclear starburst (Bunker et al. 2023; Álvarez-Márquez et al. 2025). Finally, note that, there is no detection of high excitation UV/optical narrow lines typical of Seyfert 2 AGNs, thus reinforcing the idea, even if present, a typical Seyfert 2 is not contributing to the UV and optical spectrum of U26185.

U26185 shows extremely low excitation conditions as indicated by the R3 and O32 line ratios (see Table 3 and figure 3). The ionization parameter ( $\log U$ ) corresponds to a low value of  $-2.6\pm0.2$  and  $-2.5\pm0.1$ , as derived from the SED-fitting and the O32- $\log U$  relation (Díaz et al. 2000), respectively. The different optical line diagnostics place U26185 as an outlier relative to EoR ( $z \sim 6-9$ ) and other pre-EoR ( $z > 9$ ) sources, including star-forming galaxies, AGNs, composite systems, and (broad-line) little red dots (LRDs; see Figure 3). In addition, it is worth pointing out the large difference in the optical line ratios relative to GHz9 (Napolitano et al. 2025b) at redshift of 10.145. U26185 presents much lower ratios (e.g., O32 and R23 ratios in Figure 3) than measured in these two galaxies, identified as having a coexistent AGN and nuclear starburst. GHz9 has a similar 2-10 keV luminosity ( $\sim 1.8-3.8 \times 10^{44} \text{ erg s}^{-1}$ ) than U26185. However, GHz9 shows the presence of strong, high equivalent width, UV lines (CIV] $\lambda\lambda 1548, 1551$ , OIII] $\lambda\lambda 1661, 1666$ , CIII] $\lambda\lambda 1908$ ) observed in AGNs, and no detected in the U26185 spectrum. Therefore, this does not support the presence of a luminous AGN in U26185 as in GHz9.

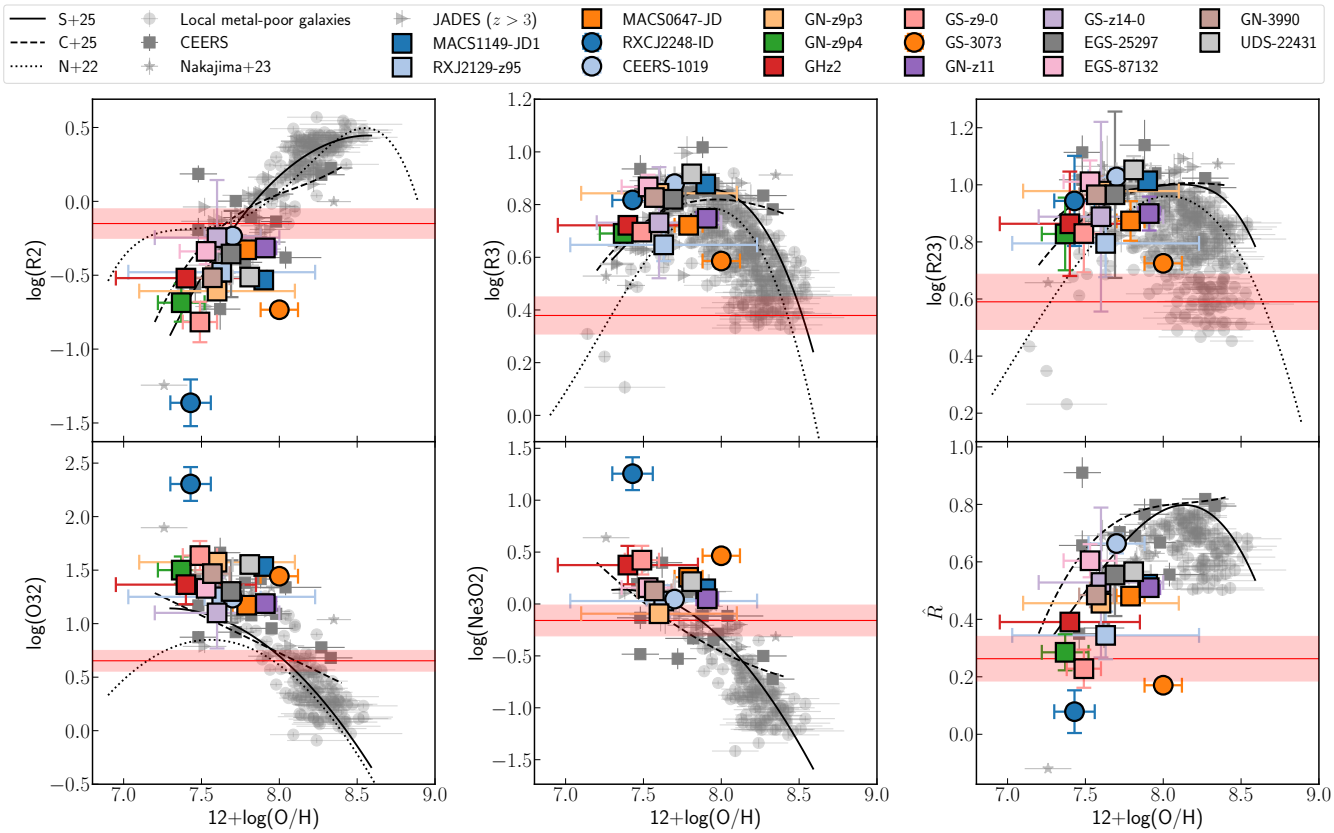


**Fig. 4.** Metallicity relations based on the different line ratios. Grey points and colored squares and circles display the samples of local metal-poor and high- $z$  galaxies, as in Fig. 3. Solid, dashed and dotted line represent the best-fit expressions derived for each line ratio by Sanders et al. (2025), Chakraborty et al. (2025) and Nakajima et al. (2022), respectively. Red horizontal line and shade mark the U26185 value and its uncertainty, respectively.

**Table 3.** Nebular metallicity based on different line-metallicity relations

Ratio	Value	S+25 (z=2–10) [7.3, 8.6]	C+25 (z=3–10) [7.2, 8.4]	N+22 (z<0.2) [6.9, 8.9]	N+22 med-EW [6.9, 8.9]
log(R2)	$-0.15 \pm 0.10$	$7.73 \pm 0.07$	$7.65 \pm 0.13$	$7.66 \pm 0.31$	$7.40 \pm 0.17$
log(R3)	$0.38 \pm 0.07$	$7.00 \pm 0.05^*$	$7.01 \pm 0.05^*$	$7.30 \pm 0.07$	$7.30 \pm 0.09$
log(R23)	$0.59 \pm 0.10$	$7.04 \pm 0.05^*$	$7.04 \pm 0.09^*$	$7.27 \pm 0.12$	$7.31 \pm 0.13$
log(O32)	$0.65 \pm 0.10$	$8.03 \pm 0.08$	$8.10 \pm 0.11$	$7.15 \pm 0.12$	$7.64 \pm 0.25$
log(Ne3O2)	$-0.16 \pm 0.15$	$7.87 \pm 0.15$	$7.66 \pm 0.15$	-	-
$\hat{R}$	$0.26 \pm 0.08$	$7.18 \pm 0.11^*$	$7.14 \pm 0.05^*$	-	-

**Notes.** S+25, C+25 and N+22 stands for Sanders et al. (2025), Chakraborty et al. (2025) and Nakajima et al. (2022), respectively. Med-EW values are derived using the relation for the  $100 < \text{EW}(\text{H}\beta)[\text{\AA}] < 200$  bin in Nakajima et al. (2022). \*: Values derived by extrapolating the expressions from S+25 and C+25 down to  $12+\log(\text{O/H})=6.9$ .

The combined UV and optical emission lines and spectral energy distribution in U26185 has no trace of the X-ray emitting AGN and appears consistent with a pure stellar origin. Hard X-ray emitting AGNs with no trace of accretion in their optical spectrum have been identified at low-redshifts (Rigby et al. 2006). In these galaxies, the obscuration in the optical of the AGN characteristics is ascribed to obscuration by dust in the host galaxy. However, there is no evidence of large amounts of dust in the host of U26185. As already mentioned in Section 4.1, deep ALMA observations have put a strong upper limit of  $5.5 \times 10^5 \text{ M}_\odot$  to the mass of cold dust in U26185 (Algera et al. 2025). This upper limit is consistent with the very low dust attenuation ( $A_{\text{V-lines}} = 0^{+0.4}_{-0.0}$  mag) measured in the stellar continuum and ISM ionized gas, and also consistent with the lack of need for

the DLA component to explain the Lyman break in this galaxy (Goulding et al. 2023). This also indicates that we are dealing with a system with a very low dust content in the host galaxy, with a dust to stellar mass ratio of less than 0.0032. However, while extremely unlikely, this amount of cold dust could still be compatible with the existence in the nucleus of U26185 of a type 2 AGN. This dust mass could be located in the circumnuclear region (i.e. inner several-tens parsecs) or in the outer regions of a dusty torus around the black hole. The median total gas mass in the dusty torus of hard X-ray selected low- $z$  Seyfert 2 is  $(3.9 \pm 5.1) \times 10^5 \text{ M}_\odot$  with column densities ( $N_H$ ) between  $10^{23}$  and  $10^{24} \text{ cm}^{-2}$  (García-Bernete et al. 2019). A very specific size and geometry with a large covering factor would be however required in order to block completely the UV-optical radiation

coming from the accretion disk and BLR, but not the observed optical emission lines. In addition, if the dust were close to the AGN, hot dust emitting at rest-frame near-infrared wavelengths would be expected and could be searched with deep MIRI imaging at longer wavelengths (10–15  $\mu\text{m}$ ).

Other than dust in the host galaxy and/or in a dusty torus, the high column-density Compton-thick obscuring material could be located in the dust-free BLR gas clouds as demonstrated by X-ray variability in low-redshift AGNs (e.g. Risaliti et al. (2002, 2011)). A similar conclusion has been derived from an X-ray study of a large sample of high-redshift ( $2 < z < 11$ ) broad- and narrow-line AGNs recently detected by JWST (Maiolino et al. 2025). According to this study, absorption by the BLR gas clouds could explain the X-ray weakness of these sources relative to the standard AGNs. This scenario predicts a covering factor of the BH and accretion disk by the BLR clouds much larger than in low-redshift AGNs. The scenario is supported by an equivalent width of the  $\text{H}\alpha$  line in these high- $z$  AGNs factor 2.6 larger than in lower redshift AGNs. However, the median  $\text{H}\alpha$  equivalent width of the JWST AGNs is 570  $\text{\AA}$ , a factor about 2.5 smaller than the value measured for U26185 (1399  $\pm$  271  $\text{\AA}$ ). Therefore, if the obscuration of the AGN in U26185 were due to the BLR clouds, U26185 would represent an extreme case of this scenario since only about 2% of the JWST AGNs have equivalent widths above 1000  $\text{\AA}$  (Maiolino et al. 2025).

In summary, all the evidence gathered so far with all the available NIRSpec and MIRI LRS spectroscopy, combined with the upper limit to the mass of cold dust in U26185, supports the idea that this galaxy is a dust-free, star-forming galaxy, not showing any evidence in its UV and optical spectrum for the presence of a Compton-thick X-ray luminous. However, a non standard, extremely young, deeply embedded, dust-poor accretion phase can not be fully excluded without further exploration. Additional data with X-ray satellites and JWST would be required to further investigate the nature of this intriguing source. Deep NIRSpec R1000 spectra would be required to search for the presence of the coronal [NeV]3426 line. High spectral resolution with MIRI MRS could help to set stronger limits on the presence of a broad  $\text{H}\alpha$  emission line associated with a type 1 AGN. In addition, deep imaging at longer wavelengths with MIRI Imager would extend the wavelength coverage into the rest-frame near-infrared range, searching for the presence of hot dust associated with an obscured AGN like recently identified in the high- $z$  source *Virgil* (Rinaldi et al. 2025).

The low significance ( $4.2\sigma$ ) of the X-ray detection in U26185 is also consistent with a source with a lower 2–10 keV luminosity ( $> 2.4 \times 10^{43} \text{ erg s}^{-1}$ ) and lower column density ( $> 1\text{e}+22 \text{ cm}^{-2}$ ; Bogdán et al. 2024). Taking the AGN scenario aside, even this hard X-ray luminosity is orders of magnitude higher than the expected value due to high-mass binary stars for a SFR of  $1.3 \text{ M}_\odot \text{ yr}^{-1}$  with a standard IMF (see X-ray-to-SFR relations in, e.g., Grimm et al. 2003; Mineo et al. 2014), and to the predictions of population III X-ray binaries (Sartorio et al. 2023). Thus, the star formation that dominates the UV and optical emission is not able to explain even the lower X-ray luminosity scenario. In addition to JWST data at longer wavelengths, deeper X-ray observations would be required to confirm the detection of the enigmatic X-ray source with a significance higher than the actual detection. U26185 is just 1 arcmin apart from the center of the galaxy cluster and the detection could be affected by the fluctuation of the X-ray background signal from the intracluster medium.

## 5.2. U26185: A metal-poor star-forming galaxy

Based on the results presented in the previous section, we rule out the presence of a classical Type 1 AGN and an obscured Seyfert 2 galaxy, as well as a LRD, challenging the presence of the supermassive active black hole ( $M_{\text{BH}} \sim 10^{7.8} \text{ M}_\odot$ ) in the nucleus of U26185, as previously inferred by Goulding et al. (2023). Therefore, U26185 exhibits the UV-to-optical spectral properties consistent with a purely star-forming galaxy. In the following, we discuss U26185 in the context of the stellar mass to metallicity relation in high- $z$  galaxies.

U26185 is the faintest UV known star-forming galaxy ( $M_{\text{UV}} = -18.8 \text{ mag}$ ) observed with MIRI spectroscopy at  $z \sim 10$ , enabled by its relatively high gravitational magnification factor ( $\mu = 4.07^{+0.03}_{-0.11}$ ). Emission-line diagnostics and SED-fitting analyses indicate intrinsic SFRs of  $1.3 \pm 0.2 \text{ M}_\odot \text{ yr}^{-1}$  ( $1.0 \text{ M}_\odot \text{ yr}^{-1}$ ) derived from  $\text{H}\alpha$  (UV continuum) corresponding to star-formation timescales of 10 Myr (100 Myr). The inferred stellar mass is  $(1.7 \pm 0.3) \times 10^8 \text{ M}_\odot$ , yielding a specific star-formation rate of  $7.6 \pm 1.2 \text{ Gyr}^{-1}$  ( $5.9 \text{ Gyr}^{-1}$ ). The SFR and stellar mass estimates identifies U26185 as a normal star-forming galaxy, placing it within a factor of less than two above the empirical main sequence of star-forming galaxies at  $z = 7\text{--}9$  (Mérida et al. 2025), and in agreement with predictions from cosmological simulations and semi-analytic models at  $z \sim 10$  (e.g., Kannan et al. 2023; Kravtsov & Belokurov 2024; Cantarella et al. 2025). U26185 therefore appears to be a representative, normal star-forming galaxy at  $z \sim 10$ , offering an opportunity to probe the typical galaxy population at this epoch, rather than focusing exclusively on extreme, UV-bright systems such as GN-z11 that occupy the bright end of the UV luminosity function (e.g., Álvarez-Márquez et al. 2025).

Figure 5 shows the position of U26185 in the stellar mass-metallicity plane, compared with galaxies at  $z \approx 4\text{--}9$  and with the known  $z > 9$  systems with metallicity measurements. It also includes empirical stellar mass-metallicity relations (MZR) at  $z < 9$ , as well as MZRs predicted by cosmological simulations at  $z \approx 9\text{--}10$ . This figure shows that approximately half of the  $z > 9$  systems fall within the scatter of lower-redshift samples, in agreement with the weak (or lack of) redshift evolution of the MZR predicted by simulations within  $z \approx 5\text{--}10$  (e.g. Ucci et al. 2023; Wilkins et al. 2023; Marszewski et al. 2024). Nevertheless, the remaining galaxies are systematically offset toward lower metallicities, potentially indicating more primeval (metal-poor) galaxies or a larger scatter in the MZR. Actually, U26185 lies among the most metal-poor galaxies observed at  $z \gtrsim 10$  to date. Its low metallicity contrasts sharply with that of UV-bright systems such as GN-z11, GS-z14-0, and MACS0647-JD at  $z > 10$ , which exhibit also significantly higher stellar masses. This difference may indicate a more advanced chemical enrichment history in these luminous systems, consistent with a more evolved nature, compared to a more representative population of normal star-forming galaxies exemplified by U26185.

Compared with simulation predictions, U26185 is in agreement with MZRs from FIRE (Ma et al. 2016) and ASTRAEUS (Ucci et al. 2023) simulations, but lies below (with a lower metallicity) of the predictions from ILLUSTRIS-TNG (Torrey et al. 2019) and FIRE-2 (Marszewski et al. 2024). It is worth noting, however, that the simulations predict a high scatter at relatively low stellar masses ( $M_\star \lesssim 10^{8.5} \text{ M}_\odot$ ; Marszewski et al. 2024), which could explain the differences between the inferred metallicity and the simulations' predictions. Larger sample of galaxies at  $z \gtrsim 10$  with different stellar masses and precise metal-

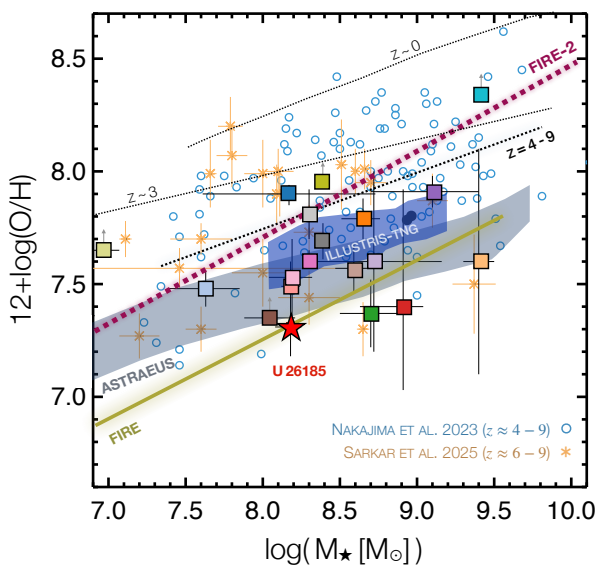


**Fig. 5.** The stellar mass-metallicity plane. The dotted black lines represent the observationally inferred relationships at  $z \approx 0.08$  (Curti et al. 2020),  $z \approx 3$  (Li et al. 2023), and  $z \approx 4 - 9$  (Nakajima et al. 2023; Curti et al. 2024; Sarkar et al. 2025). Squares represent  $z > 9$  galaxies with NIRSpec and/or MIRI detections (color coded following Figure 3). The red star is, U26185, as constrained in this work. For comparison, we also include  $z \sim 9 - 10$  predictions from simulations as follows: FIRE (Ma et al. 2016), ILLUSTRIS-TNG (Torrey et al. 2019), ASTRAEUS (Ucci et al. 2023), FIRE-2 (Marszewski et al. 2024).

licity measurements would be needed to put strong constraints on the redshift evolution of the MZR.

U26185 seems thus to be representative of a population of relatively low-mass ( $M_\star \sim 10^8 M_\odot$ ) galaxies and, while it seems to lie on the expected main-sequence of star-forming galaxies, its low metallicity (being one of the most metal-poor galaxy identified at  $z > 10$ ), indicates that it might be in an earlier evolutionary phase than other brighter  $z \gtrsim 10$  systems. It represents one of the first cases in which JWST has constrained the rest-frame optical spectrum of this otherwise hidden population of faint galaxies, made accessible by gravitational lensing despite their intrinsically low luminosities. The PRISMS program will increase the number of these faint sources and provide a valuable dataset to test the redshift evolution of the MZR in the earliest epochs of galaxy formation.

## 6. Summary and conclusions

This work presents the first results of the JWST cycle 4 PRISMS (PRImordial galaxy Survey with MIRI Spectroscopy; ID 8051) program, aimed at the characterization of the rest-frame optical spectra of a large sample of ten sources representative of intermediate UV-luminosity galaxies ( $-20.5 < M_{UV} [\text{mag}] < -17.6$ ) at redshifts of about 10, i.e. at 500 Myr after the Big Bang.

We report deep (13.9 hours) MIRI Low-Resolution Spectroscopy of the gravitationally lensed ( $\mu = 4.07$ ) galaxy U26185 at a redshift of  $z = 10.054 \pm 0.011$ . It is a faint UV galaxy ( $M_{UV} = -18.83 \pm 0.07$  mag) previously identified as a X-ray luminous AGN. We probe its rest-frame optical spectrum, detecting the  $H\beta + [\text{O III}] \lambda\lambda 4960, 5008 \text{\AA}$  complex and  $H\alpha$  emission-line with signal-to-noise ratios of 10 and 8, respectively. In addition, we detect continuum emission at rest-frame wavelengths of

0.45 and  $0.57 \mu\text{m}$  with signal-to-noise ratios of 6–7 when stacking multiple spectral elements, and we place strong upper-limits on the continuum at  $0.7 \mu\text{m}$ .

The combination of the MIRI LRS spectrum with previously reported NIRCam photometry, NIRSpec spectroscopy, and ALMA [OIII]88  $\mu\text{m}$  line and 90  $\mu\text{m}$  continuum observations allows us to investigate the star-formation history, the physical properties of the interstellar medium, and the nature of the ionization source. The main results are summarized below:

- U26185 is characterized by a star-formation history composed of two distinct stellar populations. The more mature component has a mass-weighted age of  $65 \pm 20$  Myr and a stellar mass of  $(1.5 \pm 0.3) \times 10^8 M_\odot$ , indicating that the majority of the galaxy’s stars formed around redshift  $z \sim 11$ . The young stellar population contributes  $\sim 10\%$  of the total stellar mass, with a mass of  $(1.7 \pm 0.4) \times 10^7 M_\odot$  and an age of  $7 \pm 3$  Myr. The ongoing burst is characterized by a star-formation rate of  $1.3 \pm 0.2 M_\odot \text{ yr}^{-1}$  and a specific star-formation of  $7.6 \pm 1.2 \text{ Gyr}^{-1}$ . The star-formation rate and total stellar mass locate U26185 in the main sequence of star-forming galaxies at  $z \sim 10$ , as predicted by simulations.
- The ionizing photon production efficiency is  $\log(\xi_{\text{ion}}) = 25.50 \pm 0.06 \text{ Hz erg}^{-1}$ , in agreement with sources identified in the Epoch of Reionization and beyond. U26185 is also characterized by a very high  $H\alpha$  equivalent width,  $\text{EW}(H\alpha) = 1399 \pm 271 \text{\AA}$ , compatible with the presence of stellar population ages of  $\sim 4 - 6$  Myr, for an instantaneous burst. Both, high ionizing photon production efficiency and  $\text{EW}(H\alpha)$ , reinforce the presence of a massive ( $\sim 10^7 M_\odot$ ) star-forming burst with ages at their maximum photon production efficiency and ionization.
- U26185 has negligible or zero dust attenuation ( $A_{V-\text{lines}} = 0^{+0.4}_{-0.0} \text{ mag}$ ). Consistently, SED-fitting analysis yield stellar+nebular dust attenuations compatible with the Balmer decrements, with a best value of  $A_{V-\text{SED}} = 0.20 \pm 0.09 \text{ mag}$ .
- The available emission line ratios (R2, R3, R23, O32, Ne2O2, and  $\hat{R}$ ) locate U26185 as the lowest excitation ( $\log(U) = -2.5 \pm 0.1$ ) source, as well as the most metal-poor ( $Z = 0.04 \pm 0.02 Z_\odot$ ) galaxy, identified so far at redshifts above 9.
- The emission line ratios and UV-to-optical continuum, traced by the new MIRI LRS and the ancillary NIRSpec spectra, are consistent with a stellar origin. The extremely low excitation/ionization traced by the line ratios and the high equivalent width of the  $H\alpha$  line do not show any evidence for the presence of the X-ray luminous AGN previously identified in this galaxy. This, together with the measured low nebular and stellar extinction, consistent with zero, and the low upper limit to the cold dust mass measured by ALMA observations, does not support the presence of a massive, Compton-thick, standard active black hole, either obscured by a dusty torus, or by the dust-free BLR gas clouds. Additional MIRI data are needed to further prove or discard the presence of a luminous Compton-thick AGN in this galaxy. Deep MIRI high resolution spectroscopy is required to search for a faint BLR traced by a broad  $H\alpha$  emission line, and deep MIRI imaging at wavelengths above  $10 \mu\text{m}$  would trace hot dust emission in the (circum)nuclear regions around an AGN. In addition, deeper X-ray imaging is required to increase the significance of the X-ray detection (currently at a significance of  $4.2\sigma$ ) and therefore confirm, or discard, the presence of the X-ray luminous AGN.

- The metallicity and stellar mass of U26185 is consistent with the stellar mass–metallicity predictions from some cosmological simulations (FIRE, ASTRAEUS) while clearly deviating from others (ILLUSTRIS-TNG and FIRE-2). U26185 lies among the most metal-poor galaxies known at  $z > 9$ . Their metallicity and stellar mass are significantly lower than those of UV-bright systems such as GN-z11 and GS-z14-0, therefore, probing a different (unexplored) regime in the stellar mass–metallicity relation at redshift of about 10.

Conclusively, U26185 seems thus to be representative of a population of relatively low-mass ( $M_\star \sim 10^8 M_\odot$ ), normal star-forming galaxies and, while it seems to lie on the expected main-sequence of star-forming galaxies, its low metallicity indicates that it might be in an earlier evolutionary phase than other UV-bright systems at  $z \gtrsim 10$ . It represents one of the first cases in which JWST has constrained the rest-frame optical spectrum of this otherwise hidden population of faint galaxies, made accessible by gravitational lensing despite their intrinsically low-luminosities. The PRISMS program will increase the number of these faint sources and provide a valuable dataset to investigate the stellar populations, physical properties of the interstellar medium, and nature of the ionized source of primordial galaxies, just 500 Myr after the Big Bang.

**Acknowledgements.** The authors would like to thank Almudena Alonso-Herrero and Ismael García-Bernete for discussions about AGNs and mechanisms for obscuring their radiation. J.A.-M., C.P.-J., C.B.-P., B.R.P. acknowledge support by grant PID2024-158856NA-I00. J.A.-M., L.C., C.P.-J., C.B.-P., B.R.P. acknowledge support by grant PIB2021-127718NB-I00, P.G.P.-G. acknowledges support from grant PID2022-139567NB-I00 from the Spanish Ministry of Science and Innovation/State Agency of Research MCIN/AEI/10.13039/501100011033 and by “ERDF A way of making Europe”. J.A.-M., L.C., C.P.-J., C.B.-P., P.G.P.-G. acknowledge support by grant CSIC/BILATERALES2025/BIUSP25022. L.A.B. acknowledges support from the Dutch Research Council (NWO) under grant VI.Veni.242.055 (<https://doi.org/10.61686/LAJVP77714>). M.C. acknowledges INAF GO Grant 2024 “Revealing the nature of bright galaxies at cosmic dawn with deep JWST spectroscopy”. T.H. was supported by JSPS KAKENHI 25K0020. Y.H. acknowledges support from the Japan Society for the Promotion of Science (JSPS) Grant-in-Aid for Scientific Research (24H00245), the JSPS Core-to-Core Program (JPJSCCA20210003), and the JSPS International Leading Research (22K21349). Y.F. is supported by JSPS KAKENHI Grant Numbers JP22K21349 and JP23K13149. D.L. was supported by research grants (VIL16599, VIL54489) from VILLUM FONDEN. The data were obtained from the Mikulski Archive for Space Telescopes at the Space Telescope Science Institute, which is operated by the Association of Universities for Research in Astronomy, Inc., under NASA contract NAS 5-03127 for JWST; and from the European JWST archive (eJWST) operated by the ESDC. This research made use of Photutils, an Astropy package for detection and photometry of astronomical sources (Bradley et al. 2022).

## References

Abdurro'uf, Larson, R. L., Coe, D., et al. 2024, ApJ, 973, 47

Akins, H. B., Casey, C. M., Lambrides, E., et al. 2025, ApJ, 991, 37

Algera, H. S. B., Weaver, J. R., Bakx, T. J. L. C., et al. 2025, arXiv e-prints, arXiv:2512.14486

Álvarez-Márquez, J., Burgarella, D., Buat, V., Ilbert, O., & Pérez-González, P. G. 2019, A&A, 630, A153

Álvarez-Márquez, J., Colina, L., Crespo Gómez, A., et al. 2024, A&A, 686, A85

Álvarez-Márquez, J., Crespo Gómez, A., Colina, L., et al. 2025, A&A, 695, A250

Álvarez-Márquez, J., Crespo Gómez, A., Colina, L., et al. 2023, A&A, 671, A105

Arrabal Haro, P., Dickinson, M., Finkelstein, S. L., et al. 2023, ApJ, 951, L22

Atek, H., Labb  , I., Furtak, L. J., et al. 2024, Nature, 626, 975

Balogh, M. L., Morris, S. L., Yee, H. K. C., Carlberg, R. G., & Ellingson, E. 1999, ApJ, 527, 54

Bezanson, R., Labbe, I., Whitaker, K. E., et al. 2024, ApJ, 974, 92

Bogd  ,   , Goulding, A. D., Natarajan, P., et al. 2024, Nature Astronomy, 8, 126

Boquien, M., Burgarella, D., Roehlly, Y., et al. 2019, A&A, 622, A103

Boyyet, K., Trenti, M., Leethochawalit, N., et al. 2023, arXiv e-prints, arXiv:2303.00306

Bradley, L., Sip  cz, B., Robitaille, T., et al. 2022, astropy/photutils: 1.5.0

Bruzual, G. & Charlot, S. 2003, MNRAS, 344, 1000

Bunker, A. J., Cameron, A. J., Curtis-Lake, E., et al. 2024, A&A, 690, A288

Bunker, A. J., Saxena, A., Cameron, A. J., et al. 2023, A&A, 677, A88

Burgarella, D., Bogdanoska, J., Nanni, A., et al. 2022, A&A, 664, A73

Burgarella, D., Buat, V., Theul  , P., et al. 2025, A&A, 699, A336

Bushouse, H., Eisenhamer, J., Dencheva, N., et al. 2025, JWST Calibration Pipeline

Calab  , A., Castellano, M., Zavala, J. A., et al. 2024, ApJ, 975, 245

Calab  , A., Pentericci, L., Feltre, A., et al. 2023, A&A, 679, A80

Calzetti, D., Armus, L., Bohlin, R. C., et al. 2000, ApJ, 533, 682

Cameron, A. J., Saxena, A., Bunker, A. J., et al. 2023, A&A, 677, A115

Cantarella, S., De Lucia, G., Fontanot, F., et al. 2025, arXiv e-prints, arXiv:2511.03787

Cardelli, J. A., Clayton, G. C., & Mathis, J. S. 1989, ApJ, 345, 245

Carniani, S., D'Eugenio, F., Ji, X., et al. 2024a, arXiv e-prints, arXiv:2409.20533

Carniani, S., Hainline, K., D'Eugenio, F., et al. 2024b, Nature, 633, 318

Castellano, M., Belfiori, D., Pentericci, L., et al. 2023a, A&A, 675, A121

Castellano, M., Fontana, A., Merlin, E., et al. 2025a, A&A, 704, A158

Castellano, M., Fontana, A., Treu, T., et al. 2023b, ApJ, 948, L14

Castellano, M., Napolitano, L., Fontana, A., et al. 2024, ApJ, 972, 143

Castellano, M., Napolitano, L., Moreschini, B., et al. 2025b, arXiv e-prints, arXiv:2512.08490

Chabrier, G. 2003, PASP, 115, 763

Chakraborty, P., Sarkar, A., Smith, R., et al. 2025, ApJ, 985, 24

Ciesla, L., Elbaz, D., Ilbert, O., et al. 2024, A&A, 686, A128

Crespo G  mez, A., Colina, L., P  rez-Gonz  lez, P. G., et al. 2025, arXiv e-prints, arXiv:2512.02997

Curti, M., Maiolino, R., Curtis-Lake, E., et al. 2024, A&A, 684, A75

Curti, M., Mannucci, F., Cresci, G., & Maiolino, R. 2020, MNRAS, 491, 944

Curti, M., Witstok, J., Jakobsen, P., et al. 2025, A&A, 697, A89

Curtis-Lake, E., Carniani, S., Cameron, A., et al. 2023, Nature Astronomy, 7, 622

Dekel, A., Sarkar, K. C., Birnboim, Y., Mandelker, N., & Li, Z. 2023, MNRAS, 523, 3201

D  az, A. I., Castellanos, M., Terlevich, E., & Luisa Garc  a-Vargas, M. 2000, MNRAS, 318, 462

Donnan, C. T., Dickinson, M., Taylor, A. J., et al. 2025, ApJ, 993, 224

Dors, O. L. 2021, MNRAS, 507, 466

Dors, O. L., Freitas-Lemes, P., Am  res, E. B., et al. 2020a, MNRAS, 492, 468

Dors, O. L., Maiolino, R., Cardaci, M. V., et al. 2020b, MNRAS, 496, 3209

Draine, B. T. & Li, A. 2007, ApJ, 657, 810

Eldridge, J. J. & Stanway, E. R. 2020, arXiv e-prints, arXiv:2005.11883

Ferrara, A., Pallottini, A., & Dayal, P. 2023, MNRAS, 522, 3986

Finkelstein, S. L., Bagley, M. B., Ferguson, H. C., et al. 2023, ApJ, 946, L13

Fudamoto, Y., Oesch, P. A., Faisst, A., et al. 2020, A&A, 643, A4

Fujimoto, S., Arrabal Haro, P., Dickinson, M., et al. 2023, ApJ, 949, L25

Fujimoto, S., Wang, B., Weaver, J. R., et al. 2024, ApJ, 977, 250

Furtak, L. J., Zitrin, A., Weaver, J. R., et al. 2023, MNRAS, 523, 4568

Garc  a-Bernete, I., Ramos Almeida, C., Alonso-Herrero, A., et al. 2019, MNRAS, 486, 4917

Goulding, A. D., Greene, J. E., Setton, D. J., et al. 2023, ApJ, 955, L24

Grimm, H.-J., Gilfanov, M., & Sunyaev, R. 2003, MNRAS, 339, 793

Harikane, Y., Ouchi, M., Oguri, M., et al. 2023, ApJS, 265, 5

Helton, J. M., Morrison, J. E., Hainline, K. N., et al. 2025, arXiv e-prints, arXiv:2512.19695

Ho, L. C., Feigelson, E. D., Townsley, L. K., et al. 2001, ApJ, 549, L51

Hsiao, T. Y.-Y., Abdurro'uf, Coe, D., et al. 2024a, ApJ, 973, 8

Hsiao, T. Y.-Y.,   lvarez-M  rquez, J., Coe, D., et al. 2024b, ApJ, 973, 81

Hsiao, T. Y.-Y., Coe, D., Abdurro'uf, et al. 2023, ApJ, 949, L34

Hutter, A., Cueto, E. R., Dayal, P., et al. 2025, A&A, 694, A254

Izotov, Y. I., Guseva, N. G., Fricke, K. J., & Henkel, C. 2019, A&A, 623, A40

Izotov, Y. I., Stasi  ska, G., Meynet, G., Guseva, N. G., & Thuan, T. X. 2006, A&A, 448, 955

Ji, X., Maiolino, R., Ferland, G., et al. 2025, MNRAS, 541, 2134

Ji, X.,   bler, H., Maiolino, R., et al. 2024, arXiv e-prints, arXiv:2404.04148

Jin, C., Ward, M., & Done, C. 2012, MNRAS, 422, 3268

Kannan, R., Springel, V., Hernquist, L., et al. 2023, MNRAS, 524, 2594

Kendrew, S., Scheithauer, S., Bouchet, P., et al. 2015, PASP, 127, 623

Komarova, L., Stefanon, M., Laza-Ramos, A., et al. 2025, arXiv e-prints, arXiv:2511.10743

Kov  cs, O. E., Bogd  ,   , Natarajan, P., et al. 2024, ApJ, 965, L21

Kravtsov, A. & Belokurov, V. 2024, arXiv e-prints, arXiv:2405.04578

Langeroodi, D. & Hjorth, J. 2024, arXiv e-prints, arXiv:2409.07455

Larson, R. L., Finkelstein, S. L., Kocevski, D. D., et al. 2023, arXiv e-prints, arXiv:2303.08918

Li, M., Cai, Z., Bian, F., et al. 2023, ApJ, 955, L18

Llerena, M., Pentericci, L., Napolitano, L., et al. 2025, A&A, 698, A302

Ma, X., Hopkins, P. F., Faucher-Giguère, C.-A., et al. 2016, MNRAS, 456, 2140

Maiolino, R., Risaliti, G., Signorini, M., et al. 2025, MNRAS, 538, 1921

Maiolino, R., Scholtz, J., Witstok, J., et al. 2024, Nature, 627, 59

Marszewski, A., Sun, G., Faucher-Giguère, C.-A., Hayward, C. C., & Feldmann, R. 2024, ApJ, 967, L41

Matthee, J., Sobral, D., Best, P., et al. 2017, MNRAS, 465, 3637

Mérida, R. M., Sawicki, M., Iyer, K. G., et al. 2025, arXiv e-prints, arXiv:2509.22871

Mineo, S., Gilfanov, M., Lehmer, B. D., Morrison, G. E., & Sunyaev, R. 2014, MNRAS, 437, 1698

Morishita, T., Roberts-Borsani, G., Treu, T., et al. 2023, ApJ, 947, L24

Morishita, T., Stiavelli, M., Grillo, C., et al. 2024, arXiv e-prints, arXiv:2402.14084

Naidu, R. P., Oesch, P. A., Brammer, G., et al. 2025, arXiv e-prints, arXiv:2505.11263

Nakajima, K., Ouchi, M., Isobe, Y., et al. 2023, ApJS, 269, 33

Nakajima, K., Ouchi, M., Xu, Y., et al. 2022, ApJS, 262, 3

Napolitano, L., Castellano, M., Pentericci, L., et al. 2025a, A&A, 693, A50

Napolitano, L., Castellano, M., Pentericci, L., et al. 2025b, ApJ, 989, 75

Noll, S., Burgarella, D., Giovannoli, E., et al. 2009, A&A, 507, 1793

Papovich, C., Simons, R. C., Estrada-Carpenter, V., et al. 2022, ApJ, 937, 22

Pei, Y. C. 1992, ApJ, 395, 130

Pérez-González, P. G., Costantin, L., Langeroodi, D., et al. 2023, ApJ, 951, L1

Pérez-González, P. G., Östlin, G., Costantin, L., et al. 2025, ApJ, 991, 179

Planck Collaboration, Aghanim, N., Akrami, Y., et al. 2020, A&A, 641, A6

Pollock, C. L., Gottumukkala, R., Heintz, K. E., et al. 2025, arXiv e-prints, arXiv:2506.15779

Price, S. H., Bezanson, R., Labbe, I., et al. 2025, ApJ, 982, 51

Prieto-Jiménez, C., Álvarez-Márquez, J., Colina, L., et al. 2025, A&A, 701, A31

Reddy, N. A., Topping, M. W., Shapley, A. E., et al. 2022, ApJ, 926, 31

Rieke, G. H., Wright, G. S., Böker, T., et al. 2015, PASP, 127, 584

Rigby, J. R., Rieke, G. H., Donley, J. L., Alonso-Herrero, A., & Pérez-González, P. G. 2006, ApJ, 645, 115

Rinaldi, P., Caputi, K. I., Costantin, L., et al. 2023, ApJ, 952, 143

Rinaldi, P., Caputi, K. I., Iani, E., et al. 2024, ApJ, 969, 12

Rinaldi, P., Pérez-González, P. G., Rieke, G. H., et al. 2025, ApJ, 994, 86

Risaliti, G., Elvis, M., & Nicastro, F. 2002, ApJ, 571, 234

Risaliti, G., Maiolino, R., & Salvati, M. 1999, ApJ, 522, 157

Risaliti, G., Nardini, E., Salvati, M., et al. 2011, MNRAS, 410, 1027

Roberts-Borsani, G., Oesch, P., Ellis, R., et al. 2025, arXiv e-prints, arXiv:2508.21708

Roberts-Borsani, G., Treu, T., Chen, W., et al. 2023, Nature, 618, 480

Roberts-Borsani, G., Treu, T., Shapley, A., et al. 2024, ApJ, 976, 193

Robertson, B. E., Tacchella, S., Johnson, B. D., et al. 2023, Nature Astronomy, 7, 611

Sanders, R. L., Shapley, A. E., Topping, M. W., et al. 2025, arXiv e-prints, arXiv:2508.10099

Sanders, R. L., Shapley, A. E., Topping, M. W., Reddy, N. A., & Brammer, G. B. 2024, ApJ, 962, 24

Sarkar, A., Chakraborty, P., Vogelsberger, M., et al. 2025, ApJ, 978, 136

Sartorio, N. S., Fialkov, A., Hartwig, T., et al. 2023, MNRAS, 521, 4039

Schaerer, D., Marques-Chaves, R., Xiao, M., & Korber, D. 2024, Discovery of a new N-emitter in the epoch of reionization

Schouws, S., Bouwens, R. J., Ormerod, K., et al. 2025, ApJ, 988, 19

Shivaei, I., Reddy, N., Rieke, G., et al. 2020, ApJ, 899, 117

Simmonds, C., Tacchella, S., Hainline, K., et al. 2024, MNRAS, 527, 6139

Stanway, E. R. & Eldridge, J. J. 2023, MNRAS, 522, 4430

Stiavelli, M., Morishita, T., Chiaberge, M., et al. 2023, ApJ, 957, L18

Storey, P. J. & Zeippen, C. J. 2000, MNRAS, 312, 813

Suess, K. A., Weaver, J. R., Price, S. H., et al. 2024, ApJ, 976, 101

Tang, M., Stark, D. P., Chen, Z., et al. 2023, MNRAS, 526, 1657

Tang, M., Stark, D. P., Mason, C. A., et al. 2025, arXiv e-prints, arXiv:2507.08245

Theios, R. L., Steidel, C. C., Strom, A. L., et al. 2019, ApJ, 871, 128

Topping, M. W., Stark, D. P., Senchyna, P., et al. 2024, MNRAS, 529, 3301

Torrey, P., Vogelsberger, M., Marinacci, F., et al. 2019, MNRAS, 484, 5587

Ucci, G., Dayal, P., Hutter, A., et al. 2023, MNRAS, 518, 3557

Weaver, J. R., Cutler, S. E., Pan, R., et al. 2024, ApJS, 270, 7

Wilkins, S. M., Vijayan, A. P., Lovell, C. C., et al. 2023, MNRAS, 518, 3935

Williams, H., Kelly, P. L., Chen, W., et al. 2023, Science, 380, 416

Witstok, J., Jakobsen, P., Maiolino, R., et al. 2025, Nature, 639, 897

Wright, G. S., Rieke, G. H., Glasse, A., et al. 2023, PASP, 135, 048003

Wright, G. S., Wright, D., Goodson, G. B., et al. 2015, PASP, 127, 595

Zamora, S., Carniani, S., Bertola, E., et al. 2025, arXiv e-prints, arXiv:2512.09022

Zavala, J. A., Bakx, T., Mitsuhashi, I., et al. 2024, ApJ, 977, L9

Zavala, J. A., Castellano, M., Akins, H. B., et al. 2025, Nature Astronomy, 9, 155